GLIA

Ddx20, DEAD box helicase 20, is essential for the differentiation of oligodendrocyte and maintenance of myelin gene expression

Journal:	*GLIA*
Manuscript ID	GLIA-00091-2021.R2
Wiley - Manuscript type:	Original Research Article
Date Submitted by the Author:	n/a
Complete List of Authors:	Simankova, Anna; Niigata University, Division of Neurobiology and Anatomy Bizen, Norihisa; Niigata University, Division of Neurobiology and Anatomy Saitoh, Sei; Fujita Health University, Department of Biomedical Molecular Sciences (Anatomy II) Ohno, Nobuhiko; Jichi Medical University Abe, Manabu; Niigata University, Brain Research Institute Sakimura, Kenji; Niigata University, Brain Research Institute Takebayashi, Hirohide; Niigata University, Division of Neurobiology and Anatomy
Topics:	Oligodendrocytes, CNS myelin, Development, Cell determination and differentiation
Techniques:	In situ hybridization, Immunocytochemistry, Electron microscopy/immunoelectron microscopy, Cellular and Developmental Neuroscience, Techniques to measure cell prolifaration, necrosis and apoptosis, PCR, Transgenic animals, Molecular Neuroscience, Deletion of genes (knockout techniques), Gene targeting
Key Words:	Ddx20/Gemin3/DP103, DEAD-box RNA helicase, myelin, oligodendrocytes, terminal differentiation

GLIA

Ddx20, DEAD box helicase 20, is essential for the differentiation of oligodendrocyte and maintenance of myelin gene expression

Anna Simankova[1#], Norihisa Bizen[1#], Sei Saitoh[2,3], Shinsuke Shibata[4], Nobuhiko Ohno[5,6], Manabu Abe[7], Kenji Sakimura[7], Hirohide Takebayashi[1,8]*

[#] These authors contributed equally to this work.

[1]Division of Neurobiology and Anatomy, Graduate School of Medical and Dental Sciences, Niigata University, Niigata 951-8510, Japan.

[2]Section of Electron Microscopy, Supportive Center for Brain Research, National Institute for Physiological Sciences, Okazaki 444-8787, Japan.

[3]Department of Biomedical Molecular Sciences (Anatomy II), Fujita Health University School of Medicine, Toyoake 470-1192, Japan.

[4]Division of Microscopic Anatomy, Graduate School of Medical and Dental Sciences, Niigata University, Niigata 951-8510, Japan.

[5]Department of Anatomy, Division of Histology and Cell Biology, School of Medicine, Jichi Medical University, Shimotsuke 329-0498, Japan.

[6]Division of Ultrastructural Research, National Institute for Physiological Sciences, Okazaki 444-8787, Japan.

[7]Department of Animal Model Development, Brain Research Institute, Niigata University, Niigata 951-8585, Japan.

[8]Center for Coordination of Research Facilities, Niigata University, Niigata 951-8510, Japan.

Keywords: Ddx20/Gemin3/DP103, DEAD-box RNA helicase, myelin, oligodendrocytes,

terminal differentiation

Running title

Oligodendrocytes require Ddx20

Main points

1. Oligodendrocyte differentiation and maintenance of myelin gene expression are disturbed by *Ddx20* deletion in oligodendrocytes.

2. Dysregulation of myelin gene splicing and reduced MAPK activation are observed in spinal cords of the *Ddx20* cKO mice.

*Corresponding authors at: Division of Neurobiology and Anatomy, Graduate School of Medical and Dental Sciences, Niigata University Niigata 951-8510, Japan. FAX +81-25-227-0753

E-mail: takebaya@med.niigata-u.ac.jp (H. Takebayashi)

Word count

Total word count: 6453 words
Abstract: 246 words
Introduction: 788 words
Materials and Methods: 2307 words
Results: 1912 words
Discussion: 1200 words

Abstract

Oligodendrocytes form myelin sheaths that surround axons, contributing to saltatory conduction and proper central nervous system (CNS) function. Oligodendrocyte progenitor cells (OPCs) are generated during the embryonic stage and differentiate into myelinating oligodendrocytes postnatally. Ddx20 is a multifunctional, DEAD-box helicase involved in multiple cellular processes, including transcription, splicing, microRNA biogenesis, and translation. Although defects in each of these processes result in abnormal oligodendrocyte differentiation and myelination, the involvement of Ddx20 in oligodendrocyte terminal differentiation remains unknown. To address this question, we used *Mbp-Cre* mice to generate *Ddx20* conditional knockout (cKO) mice to allow for the deletion of *Ddx20* from mature oligodendrocytes. *Mbp-Cre;Ddx20* cKO mice demonstrated small body sizes, behavioral abnormalities, muscle weakness, and short lifespans, with mortality by the age of 2 months old. Histological analyses demonstrated significant reductions in the number of mature oligodendrocytes and drastic reductions in the expression levels of myelin-associated mRNAs, such as *Mbp* and *Plp* at postnatal day 42. The number of OPCs did not change. A thin myelin layer was observed for large-diameter axons in *Ddx20* cKO mice, based on electron microscopic analysis. A bromodeoxyuridine (BrdU) labeling experiment demonstrated that terminal differentiation was perturbed from ages 2 weeks to 7 weeks in the CNS of *Mbp-Cre;Ddx20* cKO mice. The activation of mitogen-activated protein (MAP) kinase, which promotes myelination, was downregulated in the *Ddx20* cKO mice based on immunohistochemical detection. These results indicate that Ddx20 is an essential factor for terminal differentiation of oligodendrocytes and maintenance of myelin gene expression.

1. INTRODUCTION

The myelin sheath is a lipid-rich structure that surrounds axons and contributes to saltatory conduction, increasing the speed of action potential propagation and permitting the rapid transfer of information over long distances (Lemke, 1988; Peles & Salzer, 2000). Oligodendrocytes form myelin sheaths in the central nervous system (CNS), whereas Schwann cells perform this role in the peripheral nervous system (PNS), and oligodendrocytes may also be involved in the metabolic support of axons through the provision of lactate (Lee et al., 2012; Mot, Depp, & Nave, 2018). Myelination is a finely orchestrated process controlled by multiple factors, including extracellular signaling molecules and intracellular signaling pathways (Jessen & Mirsky, 2008). Disorders of dysmyelination and demyelination have been identified at both the CNS and PNS levels (Berger, Moser, & Forss-Petter, 2001; Jessen & Mirsky, 2008; Mahad, Trapp, & Lassmann, 2015; Nave, Sereda, & Ehrenreich, 2007), and understanding myelination mechanism may improve interventions for the treatment of these diseases by identifying strategies for the promotion of myelinating processes (Franklin & ffrench-Constant, 2008).

During embryonic development, oligodendrocyte progenitor cells (OPCs) are generated in multiple restricted domains of the embryonic neural tube, after which they migrate throughout the entire neural tube (Cai et al., 2005; Spassky et al., 1998; Vallstedt, Klos, & Ericson, 2005). The terminal differentiation from OPCs to mature oligodendrocytes occurs during the postnatal stage (Takebayashi & Ikenaka, 2015). Recently, OPCs were found to continue producing mature oligodendrocytes, even in the adult brain (Dimou, Simon, Kirchhoff, Takebayashi, & Götz, 2008; Rivers et al., 2008). Both *in vitro* and *in vivo* studies have suggested that neuronal activity

promotes OPC proliferation and adaptive myelination in the mammalian brain (Barres & Raff, 1993; Etxeberria et al., 2006; Gibson et al., 2014; Wake, Lee, & Fields, 2011), which might be involved in motor-skill learning (Xiao et al., 2016). Oligodendrocyte development is regulated by multiple intracellular factors in response to extracellular signaling. Some transcription factors are known to be involved in OPC specification or oligodendrocyte terminal differentiation; for example, Olig2 is involved in OPC specification (Lu et al., 2002; Takebayashi et al., 2002; Zhou et al., 2002), whereas Myrf (Emery et al., 2009) and Sox10 (Stolt et al., 2002) are involved in the transcription of myelin-related genes. MicroRNAs (miRNAs), which regulate translational efficiency and mRNA stability, are also essential for proper oligodendrocyte development (Zhao et al., 2010). The regulation of RNA splicing is also critical for oligodendrogenesis (Wang et al., 2008; Darbelli, Choquet, Richard, & Kleinman, 2017). Defects in any of these cellular processes have been demonstrated to results in abnormal oligodendrocyte differentiation and myelination.

The DEAD-box protein, Ddx20 (also known as Gemin3 or DP103), regulates multiple biological processes, including transcription, mRNA splicing, and translation. Ddx20 has been reported to negatively regulate the Egr2 (Krox20) transcription factor-mediated gene expression of myelin protein zero (*Mpz*) during the Schwann cell myelination (Gillian & Svaren, 2004; LeBlanc, Jang, Ward, Wrabetz, & Svaren, 2006). Ddx20 is a major component of the survival motor neuron (SMN) complex, which is essential for the regulation of RNA splicing (Charroux et al., 1999; Gubitz, Feng, & Dreyfuss, 2004). Importantly, mutations in SMN proteins, identified in spinal muscular atrophy (SMA) patients, result in significantly reduced

interactions with Ddx20 (Charroux et al., 1999). Ddx20 regulates miRNA biogenesis, and miRNAs, in turn, regulate translation. The mouse *Ddx20* gene encodes an 825-amino-acid (aa) protein, featuring a conserved RNA helicase domain (106–406 aa) and protein-protein interacting domains [369–547 aa for SMN interactions; the C-terminus region for transcription factors, such as Egr2 and steroidogenic factor 1 (SF1)] (Campbell et al., 2000; Curmi & Cauchi, 2018; Ou et al., 2001). Other Ddx family members have also been demonstrated to be involved in oligodendrogenesis: Ddx5 regulates *Mbp* mRNA translocation (Hoch-Kraft et al., 2018), and Ddx54 has been reported to regulate oligodendrocyte differentiation (Zhan et al., 2013). However, the role of Ddx20 in the terminal differentiation of oligodendrocyte remains unknown, partly because the total *Ddx20* KO mouse is lethal by the four-cell stage (Mouillet et al., 2008).

In the present study, we performed the conditional deletion of *Ddx20* gene expression in myelinating cells using *Mbp-Cre* transgenic mice. The *Mbp-Cre;Ddx20* conditional knockout (cKO) mice demonstrated small body sizes after weaning, motor abnormalities, muscle weakness, and short lifespans, with mortality by the age of 2 months. Histological analyses in the CNS demonstrated significant reductions in *Plp* and *Mbp* mRNA expression levels and the formation of thin myelin sheaths around large-diameter axons. The numbers of OPCs and *Gpr17*-positive myelinating oligodendrocytes remained intact in the CNS of *Mbp-Cre;Ddx20* cKO mice. Bromodeoxyuridine (BrdU) labeling experiments demonstrated perturbations in the differentiation from OPCs to mature oligodendrocytes. Our data indicate that Ddx20 is an essential factor for terminal differentiation of oligodendrocytes and maintenance of myelin gene expression.

2. MATERIALS AND METHODS

2.1 Animals

In the *Ddx20^{flox}* allele, two loxP sites are introduced into upstream and downstream of exon2 which contain first ATG sequence. We used *Mbp-Cre* transgenic mice (MBPCre-9 line, RBRC01461, MGI:2450460, Niwa-Kawakita, Abramowski, Kalamarides, Thomas, & Giovannini, 2000), Z/EG mice (MGI:3046177, Novak, Guo, Yang, Nagy, & Lobe, 2000). The day of birth was defined as postnatal day zero (P0). Male and female mice at 2, 3, and 6 weeks of age were used. The mice were maintained at 22 ± 2°C and 60% humidity in a 12-hr light/12-hr dark cycle under ad libitum feeding conditions. All procedures were approved by the Animal Research Committees of Niigata University and the Guide for the Care and Use of Laboratory Animals of the Institute for Laboratory Animal Research was followed.

2.2 Genotyping

Mice were genotyped by polymerase chain reaction (PCR) using a primer mix that amplifies the *Ddx20^{flox}* allele and *Mbp-Cre* allele in a single reaction mixture. The control *Ddx20^{flox}* and *Ddx20^{wt}* alleles was detected using the primers Ddx20-loxF; 5'-TAA GGC GCG CAG TTG AAT TT-3'); Ddx20-loxR; 5'-AGA TTT ACT GAT GCC ACC AG-3', which amplify 252bp fragments from *Ddx20^{wt}* allele and 352bp fragments from *Ddx20^{flox}* allele. The *Mbp-Cre* allele was detected using the primers CreP1; 5'-GCC TGC ATT ACC GGT CGA TGC ACC G-3') and CreP2; 5'-AAA TCC ATC GCT CGA CCA GTT TAG TTA CCC-3' primers, which amplify 644bp fragments (Tsujita et al. 1999). We used Quick Taq HS DyeMix (Toyobo, Japan) and the PCR machines (PCR Thermal Cycler

Dice Gradient, TaKaRa Bio; C1000 Touch Thermal Cycler, Bio-Rad). The PCR to detect *Ddx20^{flox}* and *Ddx20^{wt}* allele was performed (94°C for 2 min, 30 cycles of 94°C for 30 sec, 60°C for 30 sec, and 72°C for 30 sec, followed by 72°C for 3 min). The PCR to detect *Mbp-Cre* allele was performed under the following conditions (94°C for 2 min, 30 cycles of 94°C for 30 sec, 60°C for 30 sec, and 72°C for 1 min, followed by 72°C for 3 min).

2.3. Preparations of tissue sections

Paraffin sections and cryosections were prepared as previously described (Horie et al., 2014; Takebayashi et al., 2000), and then used for histological analyses. Mice were anesthetized with an intraperitoneal injection of a lethal dose of sodium pentobarbital (125 mg/kg body weight) and then perfused transcardially with approximately 2 mL of 0.01 M phosphate buffered saline (PBS) followed by 20–25 mL of 4% (w/v) paraformaldehyde in PBS (4% PFA). Brains and spinal cords (cervical enlargement) were removed and then immersed overnight in the 4% PFA and further incubated with 20% sucrose in PBS at 4°C overnight. On the following day, an embedding procedure was performed. For Ddx20 immunohistochemistry (IHC), we used unfixed cryosections: brains were removed and immediately frozen in Tissue-Tek OCT compound (SAKURA). For cryosections, 18-μm-thick sections were cut using cryostat (CM1850 UV, Leica; HM525 NX, Thermo Fisher Scientific). For paraffin sections, consecutive 10-μm-thick coronal sections of brains and transverse sections of the spinal cords were cut using a rotary microtome (HM 325, MICROM; RM2245, Leica Microsystems).

2.4 Immunohistochemistry (IHC)

IHC on paraffin sections was performed as previously described (Horie et al., 2020;

Takebayashi et al., 2000). Paraffin sections were deparaffinized with xylene, rehydrated through a descending ethanol series, and immersed in distilled water. Then, sections were pretreated with microwave irradiation (500 W for 5 min) in 10 mM citrate buffer (pH 6.0) and then cooled to room temperature to enhance the immunoreactivity of primary antibodies. After rinsing with Phosphate-buffered saline (PBS) for 15 min, the sections were incubated with the primary antibodies diluted with 0.5% skimmed milk (Wako, Osaka, Japan) in PBST (0.1% TritonX-100 in PBS) overnight at 4°C. After washing with PBS for 15 min, the sections were incubated in 0.5% skimmed milk in PBST containing secondary antibodies [peroxidase-labeled anti-mouse, anti-rabbit IgG (1:200, MBL, Nagoya, Japan) or peroxidase-labeled anti-rat IgG (1:200, DAKO)], for 1 hour at 37°C, and rinsed in distilled water for 15 min. Immunoreactivity was visualized in 50 mM Tris buffer, pH 7.4, containing 0.01% diaminobenzidine tetrahydrochloride (DAB) and 0.01% hydrogen peroxide for 5–15 min at 37°C. Sections were dehydrate through ethanol and xylene and then coverslipped.

For fluorescent IHC, sections were initially rinsed in PBS and treated 10mM citrate buffer (pH6.0) at 100°C for 5 min. After washing with PBS for 15 min, the sections were incubated with 10% goat serum in PBST for permeabilization and blocking. Afterwards, the sections were further incubated with primary antibodies in PBST containing 10% goat serum overnight at 4°C. After rinsing with PBST for 15 min, the sections were incubated with secondary antibodies conjugated to Alexa Fluor488 or Alexa Fluor594-conjugated anti-rabbit, anti-mouse or anti-rat IgG (Invitrogen, 1:1000, USA) for 60 min at 37°C. After rinsing with PBS for 15 min, the sections were incubated with 4′,6-diamidino-2-phenylindole (DAPI, 1 μg/ml, Dojindo) for 10 min, then washed in the PBS for 10 min.

Following primary antibodies and dilutions were used for IHC: mouse monoclonal Olig2

antibody (1:500, clone, 211F1.1, Cat#MABN50, Merck Millipore), rabbit polyclonal anti-NG2 antibody (1:500, Cat#AB5320, Merck Millipore), mouse monoclonal CC1 antibody (1:500, Cat#NB600-1021, Novus Biologicals), rat monoclonal anti-proteolipid protein (PLP) antibody (1:50, clone AA3; Yamamura, Konola, Wekerle, & Lees, 1991), rat monoclonal anti-myelin basic protein (MBP) (1:100, clone 12, Cat#ab7349, Abcam), rabbit polyclonal anti-MBP antibody (1:2,000, Cat#16141, IBL), rabbit polyclonal anti-glial fibrillary acidic protein (GFAP) (1:1,000, Cat#Z0334, DAKO; 1:10, Cat#422251, Nichirei), mouse monoclonal anti-GFAP antibody (1:500, Cat#75-240, NeuroMab), mouse monoclonal glutamine synthetase (GS) antibody (1:300, clone 6/Glutamine Synthetase, Cat#610517, BD Transduction Laboratories), mouse monoclonal anti-NeuN antibody (1:200, Cat#MAB377, Merck Millipore), rabbit polyclonal anti-Iba1 (1:2,000, Cat#019-19741, WAKO), rat monoclonal anti-CD68 antibody (1:200, Cat#MCA1957T, Bio-Rad), rabbit monoclonal anti-CD11b (1:10,000, EPR1344, Cat#ab133357, Abcam), rabbit polyclonal anti-Ddx20 (1:100, homemade antibody), rabbit monoclonal anti-cleaved caspase-3 (1:800, Cat#9664, Cell Signaling Technology), rat monoclonal anti-BrdU (1:300, Cat#ab6326, Abcam), rat monoclonal anti-green fluorescent protein (GFP) antibody (1:2,000, clone GF090R, Nacalai Tesque), rabbit polyclonal anti-GFP antibody (1:30,000, Cat#598, MBL), chick polyclonal GFP antibody (1:1,000, Cat#GFP-1020, Aves Labs), and rabbit polyclonal anti-phosho-p44/42 MAPK (Erk1/2) (Thr202/Tyr204) kinase (1:600, Cat#9101, Cell Signaling Technology).

Cell apoptosis was detected using the DeadEnd Colorimetric TUNEL System (Cat#G7360, Promega).

Images were taken with a microscope (BX53, Olympus) connected with a CCD camera (DP74; Olympus), or a confocal microscope (FV1200, Olympus).

2.5 In situ hybridization

In situ hybridization (ISH) was performed on paraffin sections. The deparaffinized sections were rehydrated in ethanol and rinsed with PBS. The sections were fixed in 4% PFA. Following washing with PBS twice, the sections were treated with 1 μg/mL proteinase K in Tris-based buffer [50 mM Tris-HCl (pH 7.6), 5 mM EDTA] for 60 min, and then rinsed in PBS. After fixation in 4% PFA in PBS and acetylation in 0.1 M triethanolamine (pH 8.0) containing 0.25% acetic anhydride for 10 min, the sections were prehybridized at 65°C for 3 h with a hybridization solution [50% formamide, 5 x saline sodium citrate (SSC) (1 x SSC is 0.15 M NaCl, 0.015 M sodium citrate in diethylpyrocarbonate-treated water), 0.2 mg/mL yeast tRNA, 0.1 mg/mL heparin, 1 x Denhardt's solution, 0.2% Tween 20, 0.1% CHAPS, and 5 mM EDTA]. The sections were then incubated with a hybridization solution containing diluted Digoxigenin (DIG)-labeled RNA probe at 65°C overnight.

The hybridized sections were washed three times with 1 x SSC and 50% formamide at 65°C for 15 min (wash I) and 30 min (wash II), and with 0.1 x SSC at 65°C for 30 min (wash III). The sections were washed twice in maleic acid buffer [0.1 M maleic acid (pH 7.5), 0.15 M NaCl and 0.1% Tween 20] for 30 min at room temperature and incubated with alkaline phosphatase-conjugated sheep anti-DIG antibody (1:2,000, Roche Diagnostics, Manheim, Germany) in overnight at 4°C. They were then washed in maleic acid buffer three times for 30 min each, and incubated with the color development solution [50 μg/mL 4-nitro blue tetrazolium chloride and 175 μg/mL 5-bromo-4-chloro-3-indolyl-phosphate (Roche Diagnostics)] in alkaline phosphatase buffer [0.1 M Tris-HCl (pH 9.5), 0.05 M $MgCl_2$, 0.1 M NaCl and 0.1% Tween 20] for

3–10 h in the dark. The following probes generated from mouse cDNA were used: *Plp* (Kagawa et al., 1994); *Mbp* (BC004704, nt 544-1975); *Pdgfrα* (Ma, Matsumoto, Tanaka, Takebayashi, & Ikenaka, 2006); *Gpr17* (BC070439, nt 270-945); *Gfap* (BC139357, nt 157-1426). Sections were counterstained by nuclear fast red (Fluka).

2.6 Western blot analysis

Proteins were extracted from the corpus callosum and the cervical spinal cord in RIPA buffer [50 mM Tris-HCl (pH 8.0), 150 mM NaCl, 1% NP-40, 0.5% Sodium Deoxycholate, 0.1% SDS, protease inhibitor cocktail (Complete Mini; Roche, Mannheim, Germany), and phosphatase inhibitor cocktail (PhosSTOP EASYpack; Roche)]. The lysates were sonicated by BioRuptor II (Cosmo Bio, Japan) and then centrifuged at 15,000 rpm for 15 min at 4°C. The supernatants were then collected. Protein concentrations were determined using BCA Protein assay kit (TaKaRa Bio, Japan). The samples were boiled in Sodium dodecyl sulfate (SDS) sample buffer [2% SDS, 50mM Tris-HCl (pH6.8), 10% glycerol, 6% β-mercaptoethanol, 0.01% bromophenol blue] for 5 min at 95°C. The denatured lysates were separated by electrophoresis (24mA for 75 min) in 5-20% SuperSep™ Ace agarose gels (Fujifilm Wako Pure Chemical Corp., Japan) and transferred to Hybond-P PVDF 0.45 (GE Healthcare, IL, USA; 250 mA for 100 min). Following blocking with 2% skim milk in TBST (25mM Tris-HCl, 137mM NaCl, 2.7mM KCl, 0.05% Tween 20, finally adjusted to pH7.5), the membrane was incubated with rabbit polyclonal anti-GFAP (1:1,000, Nichirei, Japan), rabbit polyclonal anti-MBP (1:1,000, IBL), mouse monoclonal anti-β-actin (1:1,000, AC-15, Sigma) overnight at 4°C. After washing with TBST for 5 min three times, the membrane was reacted with the secondary antibody conjugated to horseradish peroxidase (1:2,000, Cell Signaling Technology).

Immunoreactivity was visualized by Western Lightning Plus-ECL enhanced chemiluminescence substrate (PerkinElmer, MA, USA) or ImmunoStar LD (Fujifilm Wako Pure Chemical Corp.). Images were acquired using the C-DiGit blot scanner (LI-COR Biosciences, NE, USA). Signal intensities from immunoreactive bands were determined by densitometric measurement using ImageJ software (https://imagej.nih.gov/ij/).

2.7. BrdU labeling experiment

For labeling of proliferating cells, BrdU experiment was performed as previously described (Bu, Banki, Wu, & Nishiyama, 2004). 5′-Bromo-2-deoxyuridine (BrdU; Sigma-Aldrich, St. Louis, MO) was intraperitoneally injected into control and *Ddx20* cKO mice (n=3 mice per each genotype; 50 mg/kg in saline). In short-term labeling experiment, BrdU was injected once at postnatal day 14 (P14) and then mice were sacrificed 6 hours later. In the long-term labeling experiment, BrdU was injected at three successive days (P13, P14 and P15), and then mice were sacrificed at postnatal day 42 (P42).

2.8. Reverse transcription-quantitative PCR (RT-qPCR) and semi-quantitative RT-PCR

RT-qPCR was performed as described previously (Hayakawa-Yano et al., 2017) with minor modification. Briefly, total RNA was extracted from cervical spinal cord of 21 and 42 postnatal days (P21 and P42) mice and corpus callosum of P42 mice using RNeasy Mini Kit (Qiagen). One μg total RNA was reverse transcribed by SuperScript III First-Strand Synthesis System (Thermo Fisher Scientific). The RT-qPCR was performed using

StepOnePlus real-time PCR detection system (Applied Biosystems). The results were obtained by the ΔΔCt method. The mRNA levels of *Pdgfrα*, *Olig2*, *Mbp*, and *Plp* were normalized to the mRNA level of the house-keeping gene *Actb*. The primer sequences are as following: *Olig2* (*Olig2 F* 5′-TCC CCA GAA CCC GAT GAT CTT-3′; *Olig2 R* 5′-CGT GGA CGA GGA CAC AGT-3′); *Pdgfrα* (*Pdgfrα F* 5′-AGA GTT ACA CGT TTG AGC TGT C-3′; *Pdgfrα R* 5′-GTC CCT CCA CGC TAC TCC T-3′); *Mbp* (*Mbp F* 5′-AAT CGG CTC ACA AGG GAT TCA-3′; *Mbp R* 5′-TCC TCC CAG CTT AAA GAT TTT GG-3′); *Plp* (*Plp F* 5′-TGA GCG CAA CGG TAA CAG G-3′; *Plp R* 5′-TTC CCA AAC AAT GAC ACA CCC-3′). Semi-quantitative RT-PCR for detecting splicing variants was performed with PCR Thermal Cycler Dice (TaKaRa Bio). The primer sequences are as following: *Plp Ex2–Ex4* (*Plp exon2* F 5'-GGC CAC TGG ATT GTG TTT CT-3'; *Plp exon4* R 5'-GAC TGA CAG GTG GTC CAG GT-3'); *Mag Ex11–Ex13* (*Mag exon11* F 5'-GCT TCT CAG GGG GAG ACA AC-3'; *Mag exon13* R 5'- CAG GGT GTA GCT GTC CTT GG-3'); *Mbp Ex1–Ex3* (M*bp exon1* F 5'-CTC AGA GTC CGA CGA GCT TC-3'; *Mbp exon3* R 5'-GTT TTC ATC TTG GGT CCG GC-3').

2.9 Electron microscopic (EM) analysis

Electron Microscopic analysis was performed as describe previously (Morizawa et al., 2017) with minor modifications. Pieces of brain tissues fixed by the transcardial perfusion of buffered 4% PFA were immersed in 0.1M PB containing 4% PFA and 0.5% glutaraldehyde (pH 7.4) at 4 °C overnight, and 200-μm-thick slices were cut with a vibratome (VT-1000S, Leica). Tissues were washed with PBS, treated with 2% OsO_4 in 0.15% $K_4[Fe(CN)_6]$ for 1 h on ice, filtered 0.1% thiocarbohydrazide for 20 min and 2% OsO_4 for 30 min at room temperature (RT). Tissues were then treated with lead aspartate

solution at 70 °C for 30 min. Each of these treatments was followed by washing five times with double distilled water for 10–15 min. Tissues were dehydrated in a graded series of ethanol (60, 80, 90 and 95%, 5 min each), incubated with acetone dehydrated using a molecular sieve, a 1:1 mixture of resin and acetone, and 100% resin, Quetol 812 (Nisshin EM, Tokyo, Japan). The samples were placed in a mold, and cured at 70 °C for several nights. Blocks from each group were trimmed and mounted on aluminum rivets or sectioned and mounted on copper grids, and images were acquired in Merlin or Sigma (Carl Zeiss, Germany) equipped with 3View (Gatan Inc., Pleasanton, CA, USA) or HT7700 (Hitachi High Technologies, Japan). The acquired images were handled and analyzed with ImageJ and FIJI software plugins.

2.10 Statistical analyses

To determine the statistical significance between two groups, data were analyzed by *t*-test using Excel software or U-tests using Prism (GraphPad Software). For all tests, $p < 0.05$ was considered as statistically significant. Results are expressed as mean ± standard error (SE).

3. RESULTS

3.1 Assessments of cell types expressing Ddx20 and Cre recombination in mature oligodendrocytes

Ddx20 was expressed in the multiple cell types in the CNS, neurons, astrocytes and oligodendrocytes (Figure S1). To assess Cre-mediated recombination in the CNS of *Mbp-Cre* transgenic mice, we crossed female *Z/EG* reporter mice with male *Mbp-Cre* transgenic mice. Using immunohistochemistry, we confirmed the presence of

Cre recombination-mediated GFP expression in CC1-positive mature OLs in the *Mbp-Cre;Z/EG* mice at P14 (Figure S2a). No double-positive cells were observed with an astrocyte marker (GFAP), a microglial marker (Iba1), or a neuronal marker (NeuN) (Figure S2b–d).

3.2 Generation of mature oligodendrocyte-targeted *Ddx20* cKO mice

To generate a mature oligodendrocyte-targeted *Ddx20* cKO mouse, we mated female *Ddx20*$^{flox/flox}$ mice with male *Mbp-Cre;Ddx20*$^{flox/+}$ mice. Approximately one-fourth of the progeny were *Ddx20* cKO mice (*Mbp-Cre;Ddx20*$^{flox/flox}$), according to Mendelian distribution. We used *Ddx20*$^{flox/flox}$ as control mice unless otherwise described. To confirm the reduced expression of *Ddx20* mRNA and Ddx20 protein in oligodendrocyte lineage cells from *Ddx20* cKO mice, we performed ISH and IHC using a *Ddx20* antisense probe and anti-Ddx20 antibody, respectively (Figure 1). We confirmed the reduced expression of *Ddx20* mRNA in the corpus callosum of *Ddx20* cKO mice compared with that in the corpus callosum of control mice at P42 (Figure 1a and b). Furthermore, reduced number of Ddx20-positive cells were observed in the corpus callosum of *Ddx20* cKO mice compared with that of control mice (Figure 1c–e). We confirmed reduced number of Ddx20+ Olig2+ double-positive oligodendrocytes both in the gray matter and white matter of *Ddx20* cKO mice (Figure 1f–j).

3.3 Gross phenotypes of the *Ddx20* cKO mice

The *Mbp-Cre;Ddx20* cKO mice demonstrated postnatal growth retardation (Figure 2a–d). The body weights of the *Ddx20* cKO mice increased comparably to those of

control mice until P21, after which the body weights of *Ddx20* cKO mice ceased to increase. The *Ddx20* cKO mice showed impaired motor functions and held their tails high when they walked (Figure 2c). They often demonstrated a hunched-back posture at rest, starting at the age of 3 weeks. The *Ddx20* cKO mice died prematurely, and only thirty percent of *Ddx20* cKO mice survived beyond 6 weeks of age, with almost all *Ddx20* cKO mice dying by approximately 8 weeks (Figure 2e). The *Ddx20* cKO mice also demonstrated muscle weakness, as assessed by the grip strength test at P42 (Figure 2f).

3.4 Reduced numbers of mature oligodendrocytes in the *Ddx20* cKO mice

We performed histological analysis on the *Ddx20* cKO mice and found that the number of *Plp*-positive mature oligodendrocytes in the spinal cord of *Ddx20* cKO mice was significantly decreased at P42 compared with the number in control animals (Figure 3a–c). The expression level of *Mbp* mRNA was also significantly decreased in the spinal cord of *Ddx20* cKO mice at P42 compared with that in control animals (Figure 3d and e). The number of *Pdgfrα*-positive cells remained unchanged in the *Ddx20* cKO spinal cord at P42 compared to that of control animals (Figure 3f–h). At P21, *Plp* and *Mbp* mRNA expression levels appeared comparable between *Ddx20* cKO and control animals (Figure S3a–d, and i), and the number of *Pdgfrα*-positive OPCs was also similar (Figure S3e and f). qPCR data indicated a slightly increased level of *Pdgfrα* mRNA in the *Ddx20* cKO spinal cord at P21 compared with that in control animals, although it is not statistically significant (Figure S3i). These data suggest that Ddx20 is essential for the maintenance of myelin genes, such as *Plp* and *Mbp*. Because the number of OPCs remained unchanged, whereas the number of

mature oligodendrocytes decreased, these results raised a possibility that the terminal differentiation of OPCs into mature oligodendrocytes was impaired. Therefore, we performed ISH to detect *Gpr17*, which is transiently expressed in post-mitotic NG2-expressing glial cells (Boda et al., 2011). The number of *Gpr17*-positive cells in the *Ddx20* cKO spinal cord remained unchanged at both P42 (Figure 3i–k) and P21 (Figure S3g and h) compared to that of the control, which suggest that entry into terminal differentiation is not affected in the *Ddx20* cKO mice. CC1 IHC confirmed the decreased number of mature oligodendrocytes in the *Ddx20* cKO spinal cord at P42 (Figure S4a–c). PLP and MBP IHC demonstrated that positive signals for these myelin proteins could be observed in the *Ddx20* cKO spinal cord at P42 (Figure S4d-g); however, the myelin sheath structure in the *Ddx20* cKO mice appeared to be irregular in shape and varied in size (Figure S4j and l) compared with those in the control mice (Figure S4i and k). The diameters of NF-positive axons were also irregular in size in the *Ddx20* cKO mice (Figure S4j and l) compared with those in the control mice (Figure S4i and k). It is of note that the levels of MBP protein in the spinal cord were nearly equivalent between *Ddx20* cKO mice and control mice at P42 (Figure S4h). Because Ddx20 is reported to be a component of SMN complex, which regulate mRNA splicing (Curmi & Cauchi, 2018), we next performed semi-quantitative RT-PCR to check dysregulations of myelin gene splicing. We confirmed that the *Dm20* to *Plp* switch was partially perturbed in the *Ddx20* cKO spinal cords (Figure S5a and b). In addition, *Mag* exon12 exclusion rate was increased in the *Ddx20* cKO spinal cords (Figure S5c and d). However, *Mbp* exon2 inclusion rate was not changed (Figure S5e and f). These results suggest that Ddx20 regulate splicing pattern of some myelin related genes.

3.5 *Ddx20* ablation impairs the terminal differentiation of oligodendrocytes

To investigate the differentiation capacity of proliferating OPCs, we performed BrdU labeling experiments. In a short-term labeling experiment, we injected BrdU at P14 and analyzed BrdU-positive cells 6 h later (Figure 4a), which demonstrated that proliferating cells were equivalent between the spinal cords of control mice and those of *Ddx20* cKO mice (Figure 4b–d). We also analyzed BrdU+ Olig2+ double-positive oligodendrocyte lineage cells, and the numbers of these cells were equivalent between the spinal cords of control mice and those of *Ddx20* cKO mice (Figure 4e–g). This result was confirmed by counting the number of BrdU+ NG2+ double-positive OPCs (Figure S6a–g). In a long-term labeling experiment, we injected BrdU once per day, at P13, P14, and P15, and analyzed BrdU-positive cells at P42 (Figure 4h). Although it is not statistically significant, the total number of BrdU-positive cells slightly increased in the spinal cord of *Ddx20* cKO mice (Figure 4i–k); however, the number of BrdU+ CC1+ double-positive cells was dramatically decreased compared with those of control mice (Figure 4l–n). These data showed that OPCs in the spinal cord of *Ddx20* cKO mice formed at P14 produced a low number of mature oligodendrocytes at P42. Consistent with these data, BrdU+ GS+ double-positive astrocytes were increased at P42 in the spinal cord of of *Ddx20* cKO mice (Figure S7b–f), however BrdU+ Iba1+ double-positive microglia were unchanged (Figure S7g–k). The increased number of TUNEL-positive apoptotic cells were observed at P42 in the white matter of *Ddx20* cKO spinal cords (Figure S8c, d, and f), but this is not obvious in the *Ddx20* cKO spinal cords at P14 (Figure S8a, b, and e). Collectively, these data strongly suggested that OPC proliferation was intact and that the terminal

differentiation of oligodendrocytes was impaired and increased cell death occur in *Ddx20* cKO mice.

3.6 Electronic microscopic analysis of the spinal cord

The obtained IHC data prompted us to perform an electron microscopic analysis to observe the myelin ultrastructure. We found that the myelin sheath thickness associated with large-diameter axons (>2 μm) in the *Ddx20* cKO mice was significantly decreased at P42 (Figure 5b and d) compared with that of littermate control mice (Figure 5a and c). In contrast, the thickness of the myelin sheath surrounding small-diameter axons (<2 μm) appeared to remain intact in *Ddx20* cKO mice, similar to that observed in the control mice (Figure 5a–d). We confirmed these observations by performing a G ratio analysis (Figure 5e and f). To investigate early myelin formation, we also performed an electron microscopic analysis on the spinal cords at P14, and then, observed almost equivalent myelination in the *Ddx20* cKO spinal cord compared to that of control (Figure S9a and b). These results indicate that the conditional deletion of *Ddx20* from myelinating oligodendrocytes leads to the abnormal myelin structures in the large-diameter axons during the terminal differentiation.

3.7 Molecular function of Ddx20 during the terminal differentiation of oligodendrocytes

To investigate the molecular mechanisms that underlie the phenotype of thin myelin sheath formation in *Ddx20* cKO mice, we investigated the activation of Erk1/Erk2 signaling in the spinal cord because the activation of these MAP kinase (MAPK)

proteins has been suggested to be involved in determining myelin thickness (Ishii et al., 2014; Ishii et al., 2019). The phospho-p44/42 MAPK (pMAPK) IHC data demonstrated increased signals in the astrocytes of the *Ddx20* cKO spinal cord (Figure 6b) compared with that of the control (Figure 6a). In addition, when we carefully observe the spinal cord, we noticed pMAPK-positive ring structures in the white matter, which were confirmed to be myelin sheaths using double IHC for pMAPK and PLP (Figure 6c). The numbers of these ring structures surrounding NF-positive axons were dramatically reduced in spinal cords from *Ddx20* cKO mice, compared with those in the spinal cords of control mice, at P42 (Figure 6d and e). These data suggested that myelination was perturbed not only due to defects in myelin protein synthesis but also due to reductions in MAPK signaling, which regulates myelin thickness (Ishii et al., 2014).

3.8 Astrocytic and microglial responses in the spinal cords of *Mbp-Cre;Ddx20* cKO mice

Finally, we investigated astrocytic and microglial responses in the *Ddx20* cKO spinal cords at P42. Immunostaining with astrocytic markers (GFAP and GS) demonstrated a slight upregulation in GFAP signal intensity in the *Ddxc20* cKO spinal cord compared with that in the control spinal cord (Figure 7a–g), suggesting that the astrocytes had become reactive. The increase in GFAP expression in the *Ddx20* cKO spinal cord was also confirmed by Western blotting analysis (Figure 7e). These data were consistent with the astrocyte morphology staining revealed by pMAPK IHC (Figure 6a and b). It is reported that MAPK activation is involved in the astrocytic activation and proliferation in a variety of pathological conditions (Li et al., 2016;

Webster et al., 2006). In contrast, immunostaining with the microglial marker Iba1 clearly demonstrated the activated morphology of microglia (Figure 7i) in the *Ddx20* cKO spinal cord compared with that in the control spinal cord (Figure 7h). Microglial activation was also confirmed by the IHC detection of an activated microglial marker, CD11b, also known as the α-chain of macrophage antigen complex-1 (Mac-1) (Figure 7j and k; Hou et al., 2020; Zhou et al., 2018). CD11b-positive microglia are reported to be involved in the modulation of inflammation in the pathological brains (Frieler et al., 2015; Yang et al., 2018). Although reactive astrocytes were not obvious at P14 and P21 (Figure S10a–d), microglial activation in the white matter could be observed as early as P14 by both Iba1 and CD11b IHC (Figure S10e–l), which indicated that microglia might be sensitive to the abnormal terminal differentiation of *Ddx20*-KO oligodendrocytes. It is of note that the microglia with activated morphology contain myelin proteins (Figure 7l–o), suggesting phagocytosis of myelin. It is consistent with our observation of increased TUNEL-positive apoptotic cells in the *Ddx20* cKO spinal cords (Figure S8).

4. DISCUSSION

In the present study, we generated *Ddx20* cKO mice in which we were able to delete *Ddxc20* from myelinating cells. The *Ddx20* cKO mice demonstrated small body sizes after weaning, motor dysfunctions, muscle weakness, and short lifespans, with mortality within 2 months of age. Histological analyses demonstrated significant reductions in *Plp* and *Mbp* mRNA expression and the formation of thin myelin sheaths surrounding large-diameter axons. The numbers of OPCs and *Gpr17*-positive myelinating oligodendrocyte cells remained unchanged in the CNS of *Ddx20* cKO

mice compared to those in control mice. We also confirmed the perturbation of differentiation from OPCs into mature oligodendrocytes by BrdU labeling experiments. Our data indicate that Ddx20 is an essential factor for terminal differentiation of oligodendrocytes and maintenance of myelin gene expression.

4.1 The roles of RNA helicases in OL myelination and neural development

Ddx20 is a multifunctional protein with an RNA helicase domain, and one of the well-known functions of Ddx20 is the formation of the SMN complex to regulate mRNA splicing via the generation of the spliceosome. Because the proper regulation of mRNA splicing is important for oligodendrocyte differentiation (Wang et al., 2008; Darbelli, Choquet, Richard, & Kleinman, 2017), the dysregulation of splicing is likely to contribute to abnormal oligodendrocyte differentiation in *Ddx20* cKO mice. We detected dysregulation of myelin gene splicing, which was similar to that in *quaking viable* (qk^v) mice, classical demyelination mutants (Wu, Reed, Grabowski, & Artzt, 2002). Although oligodendrocyte development and CNS myelination were unaffected in SMA model mice ($Smn1^{-/-}$; *SMN2* mice) (O'Meara et al., 2017), SMN2 may be able to compensate for the loss of Smn1 function. In mouse genome, only one *Smn* gene, *Smn1*, is encoded, and *Smn1* KO mice show early lethality at the peri-implantation stage (Schrank et al., 1997). The *Ddx20* KO mice showed an even more severe phenotype (lethality by the 4-cell stage) compared with that for *Smn1* KO mice, suggesting that Ddx20 likely has additional functions, in addition to the regulation of mRNA splicing via SMN complex formation. Ddx20 has been reported to regulate transcription or translation via the direct binding to transcription factors or miRNA biogenesis (Gillian & Svaren, 2004; Hutvágner & Zamore, 2002; Mourelatos et al., 2002). Ddx20 has been reported as a major component of

miRNA-containing ribonucleoprotein complexes (miRNPs), which also contain eIF2C2 (Argonaute 2; Ago2) (Hutvágner & Zamore, 2002). We are currently unable to exclude the possibility that the dysregulation of transcription and translation also contribute to the abnormal oligodendrocyte differentiation observed in *Ddx20* cKO mice. Other members of the Ddx family have been reported to be involved in oligodendrocyte development. For example, Ddx5 binds *Mbp* mRNA and affects the post-transcriptional regulation of MBP (Hoch-Kraft et al., 2018). Ddx54 has also been implicated in myelination based on knockdown experiments (Zhan et al., 2013). Loss-of-function mutations in *DDX59* (Salpietro et al., 2018) and *DDX3X* (Kellaris et al., 2018; Lennox et al., 2020) result in human genetic diseases; therefore, some unidentified human genetic disease(s) may also be associated with hypomorphic mutations in *DDX20*.

4.2 Abnormal myelin structures in the CNS of *Ddx20* cKO mice

In the CNS of *Ddx20* cKO mice, decreased expression levels of *Mbp* and *Plp* mRNA were observed, although the expression levels of the MBP and PLP proteins appeared to be intact at P42 (Figure 3, Figure S4). We think two possible explanations for these phenomena. One explanation is regulation of mRNA stabilization by RNA binding proteins and/or trans-acting factor: stability of *Mbp* mRNA is regulated by Qki protein (Li, Zhang, Li, & Feng, 2000) and that of *Plp* mRNA is regulated by miRNA through the 3' untranslated region (Mallon & Macklin, 2002; Wang & Cambi, 2012). Since CC1 recognize Qki7 protein (Bin, Harris, & Kennedy, 2016), CC1 IHC data suggest that Qki7 is down-regulated in the *Ddx20* cKO spinal cord (Figure S4a, b). Ddx20 is also reported to be involved in miRNA biogenesis (Donker, Mouillet, Nelson, & Sadovsky, 2007; Hutvágner & Zamore, 2002). Therefore, it is possible that *Mbp* mRNA and *Plp* mRNA

are unstable in the OL of *Mbp-Cre*;*Ddx20* cKO mice. Second explanation is time lag between Cre recombination and decrease of protein amount: OPCs in the *Ddx20* cKO brain express *Ddx20* mRNA and Ddx20 protein because $Ddx20^{flox}$ allele is intact until this stage. Then, disruption of $Ddx20^{flox}$ alleles occur by Cre recombination in myelinating oligodendrocytes, which results in the downregulation of *Ddx20* mRNA and Ddx20 protein. *Mbp* and *Plp* mRNA are expressed in the *Ddx20* cKO oligodendrocytes at P14 (Figure S3). Although the amounts of mRNAs reduced rapidly, however, the amounts of myelin proteins reduced very gradually in the short term due to relatively stable features of myelin proteins (Fischer, & Morell, 1974; Sabri, Bone, & Davison,1974). The myelin sheaths surrounding large-caliber axons tended to show a more severe phenotype (thin myelin) than that observed for smaller axons, likely because larger-diameter axons tend to have thicker myelin sheaths (Sherman & Brophy, 2005), which requires the cooperation of more abundant myelin proteins. Myelin thickness has been reported to be regulated by MAPK signaling (Ishii, Furusho, Dupree, & Bansal, 2014). In the spinal cord of *Ddx20* cKO mice, reduced numbers of phospho-MAPK-positive myelin sheath structures (Figure 6c–e) were observed compared with those in the control mice. In addition, MAPK signaling has been reported to regulate OPC differentiation (Suo, Guo, He, Gu, & Xie, 2019). Since FGF and BDNF are reported to be involved in the myelination of oligodendrocyte and MAPK is one of downstream pathways of these receptors (Ishii, Furusho, Macklin, & Bansal, 2019; Peckham et al., 2016), the involvement of the FGF or BDNF signaling pathway(s) would be interesting to investigate in *Ddx20* cKO mice.

4.3 Contributing factors to the postnatal lethality of *Ddx20* cKO mice

Ddx20 cKO mice have small body weights and die within 2 months. The short lifespan observed for *Ddx20* cKO mice may be due to the abnormalities observed in mature oligodendrocytes. Previously, *jimpy* mice, which feature a mutation in *Plp*, a major myelin gene in the oligodendrocytes, were reported to die with a similarly short life span (within 4 weeks of age). However, *Ddx20* cKO mice do not demonstrate epileptic seizures or lower-limb paralysis, which are characteristic of the late stage of *jimpy* mice (Ikeda et al., 2018). In order to assess the effect of myelination of Schwann cells, we performed EM analysis on the sciatic nerve of *Ddx20* cKO and control mice at P42 and observed that it is almost comparable to control (data not shown). This result is consistent to the previous report that Cre recombination is observed in the oligodendrocyte but not in the Schwann cells of the *Mbp-Cre9* transgenic mice (Niwa-Kawakita, Abramowski, Kalamarides, Thomas, & Giovannini, 2000). *Ddx20* cKO might also have endocrine dysfunctions because of Cre recombination in the pituitary gland and testis of the *Mbp-Cre* transgenic mice (Niwa-Kawakita, Abramowski, Kalamarides, Thomas, & Giovannini, 2000). In line with these ectopic expressions, the mouse 1.3kb-*Mbp* promoter, used in the *Mbp-Cre* transgenic mice, was reported to lack regulatory elements that restrict its expression to the nervous system (Asipu, Mellor, & Blair, 2001). Therefore, we cannot rule out the possibility that abnormalities other than oligodendrocyte could also contribute to the short life span observed for *Ddx20* cKO mice.

ACKNOWLEDGEMENTS

We thank Dr. Michiko Niwa-Kawakita, Dr. Marco Giovannini and RIKEN-BRC for *MBPCre-9* transgenic mice, Dr. Corrinne G Lobe and Dr. Andras Nagy for *Z/EG* transgenic mice, and Dr. Masato Yano and Dr. Katsuhiko Ono for advices. We thank Ms.

Atsuko Imai (NIPS) and Ms. Megumi Yatabe (Jichi Medical University) for their technical support. We thank Dr. Lisa Giles from Edanz Group for editing a draft of this manuscript. We thank all members of Takebayashi lab, especially Dr. Yukiko Mori-Ochiai, Dr. Li Zhou, and Mr. Dang Minh Tran for technical supports. H. T. was supported by the Ministry of Education, Culture, Sports, Science, and Technology (MEXT) of Japan, Grant-in-Aid for Scientific Research on Innovative Areas "Glial assembly" (18H04939) and "Oscillology" (25117007), Grant-in-Aid for Exploratory Research (16K15168), Grant-in-Aid for Scientific Research (B) (18H02592), grant from the Uehara Memorial Foundation, and Interdisciplinary Joint Research Project from Brain Research Institute, Niigata University. N.B. is supported from Grant-in-Aid for Young Scientists (B) (15K18373, 17K15542). H. T. and N. B. were supported by technical support platforms for promoting research of Advanced Bioimaging Support (16H06280) and the Cooperative Study Program of National Institute for Physiological Sciences (18-129, 19-123). A. S. is supported by MEXT scholarship and a grant from Kyowakai general incorporated foundation.

CONFLICT OF INTEREST STATEMENT

The authors declare that they have no conflict of interest.

DATA AVAILABILITY STATEMENT

The data that support the findings of this study are available from the corresponding authors upon reasonable request.

ORCID

Hirohide Takebayashi, http://orcid.org/0000-0003-4493-6604

REFERENCES

Asipu, A., Mellor, A. L., & Blair, G. E. (2001). The specificity of the myelin basic protein gene promoter studied in transgenic mice. Biochemical and Biophysical Research Communications, 288, 809–818. doi: 10.1006/bbrc.2001.5837.

Barres, B. A., & Raff, M. C. (1993). Proliferation of oligodendrocyte precursor cells depends on electrical activity in axons. Nature, 361, 258–260. doi: 10.1038/361258a0.

Berger, J., Moser, H. W., & Forss-Petter, S. (2001). Leukodystrophies: recent developments in genetics, molecular biology, pathogenesis and treatment. Current Opinion in Neurology, 14, 305–312. doi: 10.1097/00019052-200106000-00007.

Bin, J. M., Harris, S. N., & Kennedy, T. E. (2016). The oligodendrocyte-specific antibody 'CC1' binds Quaking 7. Journal of Neurochemistry, 39, 181–186. doi: 10.1111/jnc.13745.

Boda, E., Viganò, F., Rosa, P., Fumagalli, M., Labat-Gest, V., Tempia, F., … Buffo, A. (2011). The GPR17 receptor in NG2 expressing cells: focus on in vivo cell maturation and participation in acute trauma and chronic damage. Glia, 59(12), 1958–1973. doi: 10.1002/glia.21237.

Bu, J., Banki, A., Wu, Q., & Nishiyama, A. (2004). Increased NG2(+) glial cell proliferation and oligodendrocyte generation in the hypomyelinating mutant shiverer. Glia, 48(1), 51–63. doi: 10.1002/glia.20055.

Cai, J., Qi, Y., Hu, X., Tan, M., Liu, Z., Zhang, J., … Qiu, M. (2005). Generation of oligodendrocyte precursor cells from mouse dorsal spinal cord independent of Nkx6 regulation and Shh signaling. Neuron, 45(1), 41–53. doi:

10.1016/j.neuron.2004.12.028.

Campbell, L., Hunter, K. M., Mohaghegh, P., Tinsley, J. M., Brasch, M. A., & Davies, K. E. (2000). Direct interaction of Smn with dp103, a putative RNA helicase: a role for Smn in transcription regulation? Human Molecular Genetics, 9(7), 1093–1100. doi: 10.1093/hmg/9.7.1093.

Charroux, B., Pellizzoni, L., Perkinson, R. A., Shevchenko, A., Mann, M., & Dreyfuss, G. (1999). Gemin3: A novel dead box protein that interacts with Smn, the spinal muscular atrophy gene product, and is a component of gems. Journal of Cell Biology, 147(6), 1181–1194. doi: 10.1083/jcb.147.6.1181.

Curmi, F., & Cauchi, R. J. (2018). The multiple lives of DEAD-box RNA helicases DP103/DDX20/Gemin3. Biochemical Society Transactions, 46(2), 329–341. doi: 10.1042/BST20180016.

Darbelli, L., Choquet, K., Richard, S., & Kleinman, C. L. (2017). Transcriptome profiling of mouse brains with qki-deficient oligodendrocytes reveals major alternative splicing defects including self-splicing. Scientific Reports, 7(1), 7554. doi: 10.1038/s41598-017-06211-1.

Dimou, L., Simon, C., Kirchhoff, F., Takebayashi, H., & Götz, M. (2008). Progeny of Olig2-expressing progenitors in the gray and white matter of the adult mouse cerebral cortex. The Journal of Neuroscience, 28(41), 10434–10442. doi: 10.1523/JNEUROSCI.2831-08.2008.

Dionne, N., Dib, S., Finsen, B., Denarier, E., Kuhlmann, T., Drouin, R., … Peterson, A. C. (2016). Functional organization of an Mbp enhancer exposes striking transcriptional regulatory diversity within myelinating glia. Glia, 64(1), 175–194. doi: 10.1002/glia.22923.

Donker, R. B., Mouillet, J. F., Nelson, D. M., & Sadovsky, Y. (2007). The expression of Argonaute2 and related microRNA biogenesis proteins in normal and hypoxic trophoblasts. Molecular Human Reproduction, 13(4), 273–279. doi: 10.1093/molehr/gam006.

Emery, B., Agalliu, D., Cahoy, J. D., Watkins, T. A., Dugas, J. C., Mulinyawe, S. B., … Barres, B. A. (2009). Myelin gene regulatory factor is a critical transcriptional regulator required for CNS myelination. Cell, 138(1), 172–185. doi: 10.1016/j.cell.2009.04.031.

Etxeberria, A., Hokanson, K. C., Dao, D. Q., Mayoral, S. R., Mei, F., Redmond, S. A., … Chan, J. R. (2006). Dynamic modulation of myelination in response to visual stimuli alters optic nerve conduction velocity. The Journal of Neuroscience, 36(26), 6937–6948. doi: 10.1523/JNEUROSCI.0908-16.2016.

Fischer, C. A., & Morell, P. (1974). Turnover of proteins in myelin and myelin-like material of mouse brain. Brain Research, 74, 51–65. doi: 10.1016/0006-8993(74)90111-5.

Franklin, R. J., & ffrench-Constant, C. (2008). Remyelination in the CNS: from biology to therapy. Nature Reviews Neuroscience, 9(11), 839–855. doi: 10.1038/nrn2480.

Frieler, R. A., Nadimpalli, S., Boland, L. K., Xie, A., Kooistra, L. J., Song, J., ... Mortensen, R. M. (2015). Depletion of macrophages in CD11b diphtheria toxin receptor mice induces brain inflammation and enhances inflammatory signaling during traumatic brain injury. Brain Research, 1624, 103–112. doi: 10.1016/j.brainres.2015.07.011.

Gibson, E. M., Purger, D., Mount, C. W., Goldstein, A. K., Lin, G. L., Wood, L. S., … Monje, M. (2014). Neuronal activity promotes oligodendrogenesis and adaptive

myelination in the mammalian brain. Science, 344(6183), 1252304. doi: 10.1126/science.1252304.

Gillian, A. L., & Svaren, J. (2004). The Ddx20/DP103 dead box protein represses transcriptional activation by Egr2/Krox-20. Journal of Biological Chemistry, 279(10), 9056–9063. doi: 10.1074/jbc.M309308200.

Gubitz, A. K., Feng W., & Dreyfuss, G. (2004). The SMN complex. Experimanetal Cell Research, 296(1), 51–56. doi: 10.1016/j.yexcr.2004.03.022.

Hayakawa-Yano, Y., Suyama, S., Nogami, M., Yugami, M., Koya, I., Furukawa, T., … Yano, M. (2017). An RNA-binding protein, Qki5, regulates embryonic neural stem cells through pre-mRNA processing in cell adhesion signaling. Genes & Development, 31, 1910–1925. doi: 10.1101/gad.300822.117.

Hoch-Kraft, P., White, R., Tenzer, S., Krämer-Albers, E. M., Trotter, J., & Gonsior, C. (2018). Dual role of the RNA Helicase DDX5 in post-transcriptional regulation of myelin basic protein in oligodendrocytes. Journal of Cell Science, 131(9), jcs204750. doi: 10.1242/jcs.204750.

Horie, M., Watanabe, K., Bepari, A. K., Nashimoto, J., Araki, K., Sano, H., … Takebayashi, H. (2014). Disruption of actin-binding domain-containing dystonin protein causes *dystonia musculorum* in mice. European Journal of Neuroscience, 40(10), 3458–3471. doi: 10.1111/ejn.12711.

Horie, M., Yoshioka, N., Kusumi, S., Sano, H., Kurose, M., Watanabe-Iida, I., … Takebayashi, H. (2020). Disruption of dystonin in Schwann cells results in late-onset neuropathy and sensory ataxia. Glia, 68(11), 2330–2344. doi: 10.1002/glia.23843.

Hou, L., Qu, X., Qiu, X., Huang, R., Zhao, X., & Wang, Q. (2020). Integrin CD11b mediates locus coeruleus noradrenergic neurodegeneration in a mouse Parkinson's

disease model. Journal of Neuroinflammation, 17(1),148. doi: 10.1186/s12974-020-01823-3.

Hutvágner, G., & Zamore, P. D. (2002). A microRNA in a multiple-turnover RNAi enzyme complex. Science, 297(5589), 2056–2060. doi: 10.1126/science.1073827.

Ikeda, M., Hossain, M. I., Zhou, L., Horie, M., Ikenaka, K., Horii, A., & Takebayashi, H. (2018). Histological detection of dynamic glial responses in the dysmyelinating Tabby-jimpy mutant brain. Anatomical Science International, 93(1), 119–127. doi: 10.1007/s12565-016-0383-5.

Ishii, A., Furusho, M., Dupree, J. L., & Bansal, R. (2014). Role of ERK1/2 MAPK signaling in the maintenance of myelin and axonal integrity in the adult CNS. The Journal of Neuroscience, 34(48), 16031–16045. doi: 10.1523/JNEUROSCI.3360-14.2014.

Ishii, A., Furusho, M., Macklin, W., & Bansal, R. (2019). Independent and cooperative roles of the Mek/ERK1/2-MAPK and PI3K/Akt/mTOR pathways during developmental myelination and in adulthood. Glia, 67(7), 1277–1295. doi: 10.1002/glia.23602.

Jessen, K. R., & Mirsky, R. (2008). Negative regulation of myelination: relevance for development, injury, and demyelinating disease. Glia, 56(14), 1552–1565. doi: 10.1002/glia.20761.

Kagawa, T., Ikenaka, K., Inoue, Y., Kuriyama, S., Tsujii, T., Nakao, J., … Mikoshiba, K. (1994). Glial cell degeneration and hypomyelination caused by overexpression of myelin proteolipid protein gene. Neuron, 13(2), 427–442. doi: 10.1016/0896-6273(94)90358-1.

Kellaris, G., Khan, K., Baig, S. M., Tsai, I. C., Zamora, F. M., Ruggieri, P., N… Katsanis,

N. (2018). A hypomorphic inherited pathogenic variant in DDX3X causes male intellectual disability with additional neurodevelopmental and neurodegenerative features. Human Genomics, 12(1), 11. doi: 10.1186/s40246-018-0141-y.

Kocur, M., Schneider, R., Pulm, A. K., Bauer, J., Kropp, S., Gliem, M., … Scheu, S. (2015). IFNβ secreted by microglia mediates clearance of myelin debris in CNS autoimmunity. Acta Neuropathologica Communications, 3, 20. doi: 10.1186/s40478-015-0192-4.

LeBlanc, S. E., Jang, S. W., Ward, R. M., Wrabetz, L., & Svaren, J. (2006). Direct regulation of myelin protein zero expression by the Egr2 transactivator. Journal of Biological Chemistry, 281(9), 5453–5460. doi: 10.1074/jbc.M512159200.

Lee, Y., Morrison, B. M., Li, Y., Lengacher, S., Farah, M. H., Hoffman, P. N., … Rothstein, J. D. (2012). Oligodendroglia metabolically support axons and contribute to neurodegeneration. Nature, 487(7408), 443–448. doi: 10.1038/nature11314.

Lemke, G. (1988). Unwrapping the genes of myelin. Neuron, 1(7), 535–543. doi: 10.1016/0896-6273(88)90103-1.

Lennox, A. L., Hoye, M. L., Jiang, R., Johnson-Kerner, B. L., Suit, L. A., Venkataramanan, S., … Sherr, E. H. (2020). Pathogenic *DDX3X* Mutations Impair RNA Metabolism and Neurogenesis during Fetal Cortical Development. Neuron, 106(3), 404–420.e8. doi: 10.1016/j.neuron.2020.01.042.

Li, D., Tong, L., Kawano, H., Liu, N., Yan, H. J., Zhao, L., & Li, H. P. (2016). Regulation and role of ERK phosphorylation in glial cells following a nigrostriatal pathway injury. Brain Research, 1648(Pt A), 90–100. doi: 10.1016/j.brainres.2016.07.008.

Li, Z., Zhang, Y., Li, D., & Feng, Y. (2000). Destabilization and mislocalization of myelin basic protein mRNAs in quaking dysmyelination lacking the QKI RNA-binding

proteins. The Journal of Neuroscience, 20(13), 4944–4953. doi: 10.1523/JNEUROSCI.20-13-04944.2000.

Lu, Q. R., Sun, T., Zhu, Z., Ma, N., Garcia, M., Stiles, C. D., & Rowitch, D. H. (2002). Common developmental requirement for Olig function indicates a motor neuron/oligodendrocyte connection. Cell, 109(1), 75–86. doi: 10.1016/s0092-8674(02)00678-5.

Ma, J., Matsumoto, M., Tanaka, K. F., Takebayashi, H., & Ikenaka, K. (2006). An animal model for late onset chronic demyelination disease caused by failed terminal differentiation of oligodendrocytes. Neuron Glia Biology, 2(2), 81–91. doi: 10.1017/S1740925X06000056.

Mahad, D. H., Trapp, B. D., & Lassmann, H. (2015). Pathological mechanisms in progressive multiple sclerosis. Lancet Neurology, 14(2), 183–193. doi: 10.1016/S1474-4422(14)70256-X.

Mallon, B. S., & Macklin, W. B. (2002). Overexpression of the 3'-untranslated region of myelin proteolipid protein mRNA leads to reduced expression of endogenous proteolipid mRNA. Neurochemical Research, 27(11), 1349–1360. doi: 10.1023/a:1021623700009.

Morizawa, Y. M., Hirayama, Y., Ohno, N., Shibata, S., Shigetomi, E., Sui, Y., … Koizumi, S. (2017). Reactive astrocytes function as phagocytes after brain ischemia via ABCA1-mediated pathway. Nature Commununications, 8(1), 28. doi: 10.1038/s41467-017-00037-1.

Mourelatos, Z., Dostie, J., Paushkin, S., Sharma, A., Charroux, B., Abel, L., … Dreyfuss, G. (2002). miRNPs: a novel class of ribonucleoproteins containing numerous microRNAs Genes & Development, 16(6), 720–728. doi: 10.1101/gad.974702.

Mot, A. I., Depp, C., & Nave, K. A. (2018). An emerging role of dysfunctional axon-oligodendrocyte coupling in neurodegenerative diseases. Dialogues in Clinical Neuroscience, 20(4), 283–292.

Mouillet, J. F., Yax, X., Ou, Q., Jin, L., Muglia, L. J., Crawford, P. A., & Sadovsky, Y. (2008). DEAD-box protein-103 (DP103, Ddx20) is essential for early embryonic development and modulates ovarian morphology and function. Endocrinology, 149 (5), 2168–2175. doi: 10.1210/en.2007-1237.

Nave, K. A., Sereda, M. W., & Ehrenreich, H. (2007). Mechanisms of disease: inherited demyelinating neuropathies—from basic to clinical research. Nature Clinical Practice Neurology. 3(8), 453–464. doi: 10.1038/ncpneuro0583.

Niwa-Kawakita, M., Abramowski, V., Kalamarides, M., Thomas, G., & Giovannini, M. (2000). Targeted expression of Cre recombinase to myelinating cells of the central nervous system in transgenic mice. Genesis, 26(2), 127–129. doi: 10.1002/(sici)1526-968x(200002)26:2<127::aid-gene8>3.0.co;2-h.

Novak, A., Guo, C., Yang, W., Nagy, A., & Lobe, C. G. (2000). Z/EG, a double reporter mouse line that expresses enhanced green fluorescent protein upon Cre-mediated excision. Genesis, 28(3–4), 147–155. doi: 10.1002/1526-968X(200011/12)28:3/4<147::AID-GENE90>3.0.CO;2-G.

O'Meara, R. W., Cummings, S. E., De Repentigny, Y., McFall, E., Michalski, J. P., Deguise, M. O., … Kothary, R. (2017). Oligodendrocyte development and CNS myelination are unaffected in a mouse model of severe spinal muscular atrophy. Human Molecular Genetics, 26(2), 282–292. doi: 10.1093/hmg/ddw385.

Ou, Q., Mouillet, J. F., Yan, X., Dorn, C., Crawford, P. A., & Sadovsky, Y. (2001). The DEAD box protein DP103 is a regulator of steroidogenic factor-1. Molecular

Endocrinology, 15(1), 69–79. doi: 10.1210/mend.15.1.0580.

Peckham, H., Giuffrida, L., Wood, R., Gonsalvez, D., Ferner, A., Kilpatrick, T. J., … Xiao J. (2016). Fyn is an intermediate kinase that BDNF utilizes to promote oligodendrocyte myelination. Glia, 64(2), 255–269. doi: 10.1002/glia.22927.

Peles, E., & Salzer, J. L. (2000). Molecular domains of myelinated axons. Current Opinion in Neurobiology, 10(5), 558–565. doi: 10.1016/s0959-4388(00)00122-7.

Rivers, L. E., Young, K. M., Rizzi, M., Jamen, F., Psachoulia, K., Wade, A., … Richardson, W. D. (2008). PDGFRA/NG2 glia generate myelinating oligodendrocytes and piriform projection neurons in adult mice. Nature Neuroscience, 11(12), 1392–1401. doi: 10.1038/nn.2220.

Sabri, M. I., Bone, A. H., & Davison, A. N. (1974). Turnover of myelin and other structural proteins in the developing rat brain. Biochemical Journal, 142, 499–507. doi:10.1042/bj1420499 pmid:4142927

Salpietro, V., Efthymiou, S., Manole, A., Maurya, B., Wiethoff, S., Ashokkumar, B., … Houlden, H. (2018). A loss-of-function homozygous mutation in DDX59 implicates a conserved DEAD-box RNA helicase in nervous system development and function. Human Mutation, 39(2), 187–192. doi: 10.1002/humu.23368.

Schrank, B., Götz, R., Gunnersen, J. M., Ure, J. M., Toyka, K. V., Smith, A. G., & Sendtner, M. (1997). Inactivation of the survival motor neuron gene, a candidate gene for human spinal muscular atrophy, leads to massive cell death in early mouse embryos. Proceedings of the National Academy of Sciences of the United States of America, 94(18), 9920–9925. doi: 10.1073/pnas.94.18.9920.

Sherman, D. L., & Brophy, P. J. (2005). Mechanisms of axon ensheathment and myelin growth. Nature Reviews Neuroscience, 6, 683–690. doi: 10.1038/nrn1743.

Spassky, N., Goujet-Zalc, C., Parmantier, E., Olivier, C., Martinez, S., Ivanova, A., … Thomas, J. L. (1998). Multiple restricted origin of oligodendrocytes. The Journal of Neuroscience, 18(20), 8331–8343. doi: 10.1523/JNEUROSCI.18-20-08331.1998.

Stolt, C. C., Rehberg, S., Ader, M., Lommes, P., Riethmacher, D., Schachner, M., … Wegner, M. (2002). Terminal differentiation of myelin-forming oligodendrocytes depends on the transcription factor Sox10. Genes & Development, 16(2),165–170. doi: 10.1101/gad.215802.

Suo, N., Guo, Y. E., He, B., Gu, H., & Xie, X. (2019). Inhibition of MAPK/ERK pathway promotes oligodendrocytes generation and recovery of demyelinating diseases. Glia, 67(7), 1320–1332. doi: 10.1002/glia.23606.

Takebayashi, H, & Ikenaka, K. (2015). Oligodendrocyte generation during mouse development. Glia, 63(8), 1350–1356. doi: 10.1002/glia.22863.

Takebayashi, H., Nabeshima, Y., Yoshida, S., Chisaka, O., Ikenaka, K., & Nabeshima, Y. (2002). The basic helix-loop-helix factor olig2 is essential for the development of motoneuron and oligodendrocyte lineages. Current Biology, 12(13), 1157–1163. doi: 10.1016/s0960-9822(02)00926-0.

Takebayashi, H., Yoshida, S., Sugimori, M., Kosako, H., Kominami, R., Nakafuku, M., & Nabeshima, Y. (2000). Dynamic expression of basic helix-loop-helix Olig family members: implication of Olig2 in neuron and oligodendrocyte differentiation and identification of a new member, Olig3. Mechanisms of Development, 99(1–2), 143–148. doi: 10.1016/s0925-4773(00)00466-4.

Tsujita, M., Mori, H., Watanabe, M., Suzuki, M., Miyazaki, J., & Mishina, M. (1999). Cerebellar granule cell-specific and inducible expression of Cre recombinase in the mouse. The Journal of Neuroscience, 19(23), 10318–10323. doi:

10.1523/JNEUROSCI.19-23-10318.1999.

Vallstedt, A., Klos, J. M., & Ericson, J. (2005). Multiple dorsoventral origins of oligodendrocyte generation in the spinal cord and hindbrain. Neuron, 45(1), 55–67. doi: 10.1016/j.neuron.2004.12.026.

Wake, H., Lee, P. R., & Fields, R. D. (2011). Control of local protein synthesis and initial events in myelination by action potentials. Science, 333(6049), 1647–1651. doi: 10.1126/science.1206998.

Wang, E., & Cambi, F. (2012). MicroRNA expression in mouse oligodendrocytes and regulation of proteolipid protein gene expression. Journal of Neuroscience Research, 90(9), 1701–1712. doi: 10.1002/jnr.23055.

Wang, E., Dimova, N., Sperle, K., Huang, Z., Lock, L., McCulloch, M. C., … Cambi, F. (2008). Deletion of a splicing enhancer disrupts PLP1/DM20 ratio and myelin stability. Experimental Neurology, 214(2), 322–330. doi: 10.1016/j.expneurol.2008.09.001.

Webster, B., Hansen, L., Adame, A., Crews, L., Torrance, M., Thal, L., & Masliah, E. (2006). Astroglial activation of extracellular-regulated kinase in early stages of Alzheimer disease. Journal of Neuropathology & Experimental Neurology, 65(2), 142–151. doi: 10.1097/01.jnen.0000199599.63204.6f.

Wu, J. I., Reed, R. B., Grabowski, P. J., & Artzt, K. (2002). Function of *quaking* in myelination: Regulation of alternative splicing. Proceedings of the National Academy of Sciences of the United States of America. 99(7), 4233–4238. doi: 10.1073/pnas.072090399.

Xiao, L., Ohayon, D., McKenzie, I. A., Sinclair-Wilson, A., Wright, J. L., Fudge, A. D., … Richardson, W. D. (2016). Rapid production of new oligodendrocytes is required in the earliest stages of motor-skill learning. Nature Neuroscience, 19(9), 1210–1217.

doi: 10.1038/nn.4351.

Yamamura, T., Konola, J. T., Wekerle, H., & Lees, M. B. (1991). Monoclonal antibodies against myelin proteolipid protein: identification and characterization of two major determinants. Journal of Neurochemistry, 57(5), 1671–1680. doi: 10.1111/j.1471-4159.1991.tb06367.x.

Yang, M., Xu, W., Wang, Y., Jiang, X., Li, Y., Yang, Y., & Yuan, H. (2018). CD11b-activated Src signal attenuates neuroinflammatory pain by orchestrating inflammatory and anti-inflammatory cytokines in microglia. Molecular Pain, 14, 1744806918808150. doi: 10.1177/1744806918808150.

Zhan, R., Yamamoto, M., Ueki, T., Yoshioka, N., Tanaka, K., Morisaki, H., … Aiso, S. (2013). A DEAD-box RNA helicase Ddx54 protein in oligodendrocytes is indispensable for myelination in the central nervous system. Journal of Neuroscience Research, 91(3), 335–348. doi: 10.1002/jnr.23162.

Zhao, X., He, X., Han, X., Yu, Y., Ye, F., Chen, Y., … Lu, Q. R. (2010). MicroRNA-mediated control of oligodendrocyte differentiation. Neuron, 65(5), 612–626. doi: 10.1016/j.neuron.2010.02.018.

Zhou, L., Hossain, M. I., Yamazaki, M., Abe, M., Natsume, R., Konno, K., … Takebayashi, H. (2018). Deletion of exons encoding carboxypeptidase domain of Nna1 results in Purkinje cell degeneration (*pcd*) phenotype. Journal of Neurochemistry, 147(4), 557–572. doi: 10.1111/jnc.14591.

Zhou, Q., & Anderson, D. J. (2002). The bHLH transcription factors OLIG2 and OLIG1 couple neuronal and glial subtype specification. Cell, 109(1), 61–73. doi: 10.1016/s0092-8674(02)00677-3.

FIGURE LEGENDS

FIGURE 1 Cre-mediated *Ddx20* deletion in the oligodendrocyte lineage.

(a–b) *Ddx20* ISH in the coronal sections of *Ddx20*$^{flox/flox}$ (control) (a) and *Mbp-Cre*;*Ddx20*$^{flox/flox}$ (*Ddx20* cKO) (b) forebrain at P42. *Ddx20* expression was markedly reduced in the corpus callosum of *Ddx20* cKO mice (b) compared with that of control mice (a, arrowheads) (n=3 mice in each genotype). (c–j) Double IHC for Ddx20 and Olig2 in the coronal section of forebrain at P42 (n=3 mice in each genotype). Ddx20 signals (green) were negative or low in the Olig2-positive cells within the corpus callosum, but positive in the neurons within the cerebral cortex. Ddx20 single positive cells in the cerebral cortex were considered as neurons based on morphology. (e,j) Bar graphs showing the number of Ddx20 positive cells (e) or Ddx20+ and Olig2+ double-positive cells (j) per section in the corpus callosum and cerebral cortex (0.05 mm^2, mean ± SEM). Statistical analysis was performed by two-tailed, unpaired *t*-test. ***, $p<0.001$. CC: corpus callosum, Cx: cortex. Scale bars: 50 μm (a,b), 100 μm (c,d, f-i). Ctrl: control, *Ddx20* cKO: *Mbp-Cre;Ddx20* cKO.

FIGURE 2 Generation of *Ddx20*^{flox} allele and retarded growth of *Mbp-Cre;Ddx20* cKO mice.

(a) Schematic illustrating the strategy for the generation of *Ddx20*^{flox} allele. Construction of alleles and vectors for the mouse *Ddx20* genes: the wild type genome, targeting vector, flox-neo allele, floxed allele, and deleted allele. Arrows indicate primers for the distinction between the wild-type allele and the *Ddx20*^{flox} allele. (b) A typical image of *Ddx20* cKO mouse and littermate control

mouse at P42. (c) A typical image of walking-*Ddx20* cKO mice and littermate control mice at P42. Red arrows indicate tail rigidity of the *Ddx20* cKO mouse. (d) Growth curves of *Ddx20* cKO mice (n = 32, a blue line) and control mice (n=33, a black line). Line plots represent mean ± SEM. (e) Kaplan-Meier survival curves of *Ddx20* cKO mice (n=11) and control mice (n=11). Of eleven *Ddx20* cKO mice, approximately 90% died within 7 weeks of age, with a peak between postnatal days 42 and 49. (f) Grip strength test of forelimb in *Ddx20* cKO mice and littermate control mice (n=10) at P42. Statistical analysis was performed by two-tailed, unpaired *t*-test (d, f) and Log-rank test (e). ***, $p<0.001$.

FIGURE 3 Decreased number of mature oligodendrocytes in the spinal cord of *Mbp-Cre;Ddx20* cKO mice.

(a,b) *Plp* ISH in the transverse sections of control (a) and *Ddx20* cKO (b) spinal cords at P42 (n=3 mice in each genotype). (c) Quantification of the number of *Plp*-positive mature OLs in the anterolateral funiculus (per 0.05 mm^2, mean ± SEM). (d,e) *Mbp* ISH in the transverse sections of control (d) and *Ddx20* cKO (e) spinal cords at P42 (n=3 mice in each genotype). Note that distribution pattern of *MBP* mRNA and that of *Plp* mRNA in the control spinal cords are different because of intracellular transport of *Mbp* mRNA. (f,g) *Pdgfrα* ISH in the transverse sections of control (f) and *Ddx20* cKO (g) spinal cords at P42 (n=3 mice in each genotype). (h) Quantification of the number of *Pdgfrα*-positive OPCs in the anterolateral funiculus (per 0.05 mm^2, mean ± SEM). (i, j) *Gpr17* ISH in the transverse sections of control (i) and *Ddx20* cKO (j) spinal cords at P42 (n=3 mice in each genotype). (k) Quantification of the number of *Gpr17*-positive myelinating OLs in the anterolateral funiculus (per 0.05 mm^2, mean ± SEM). (l) RT-qPCR data of *Plp*, *Mbp*,

Olig2 and *Pdgfra* mRNAs in the spinal cords at P42 (n=3 mice in each genotype). *Actb* was used as an internal control (mean ± SEM). Statistical analysis was performed by two-tailed, unpaired *t*-test. **, p<0.01; ***, p<0.001; n.s., not significant. Scale bars: 50 μm (a-d, f,g,i,j,l,m).

FIGURE 4 Terminal differentiation of oligodendrocyte is perturbed in the *Mbp-Cre;Ddx20* cKO mice.

(a) Diagrams of the experimental timeline for BrdU short-term administration. (b–g) Double IHC for BrdU and Olig2 in the transverse sections of control and *Ddx20* cKO spinal cords at P14 after short-term BrdU labeling experiments. Upper- and lower-panels show the images with BrdU immunostaining (b,c) and BrdU+ Olig2+ double-immunostaining (e,f), respectively. Yellow arrowheads indicate BrdU+ Olig2+ double-positive cells. Bar charts indicate the average number of BrdU-positive cells (d) or BrdU+ Olig2+ double-positive cells per spinal cord section (g, mean ± SEM, n=3 mice per group). (h) Diagrams of the experimental timeline for BrdU long-term administration. (i–n) Double IHC for BrdU and CC1 in the transverse sections of control and *Ddx20* cKO spinal cords at P42 after long-term BrdU labeling experiments. Upper- and lower-panels show the images with BrdU immunostaining (i,j) and BrdU+ CC1+ double-immunostaining (l,m), respectively. Yellow arrowheads indicate BrdU+ CC1+ double-positive cells. Bar charts indicate the average number of BrdU-positive cells (k) or BrdU+ CC1+ double-positive cells (n) per section in control (n=4 mice) and *Ddx20* cKO (n=3 mice) spinal cords (mean ± SEM). Statistical analysis was performed by two-tailed, unpaired *t*-test. **, p<0.01; n.s., not significant. Scale bars: 100 μm (b,c,e,f,i,j,l,n).

FIGURE 5 Thin myelin structure in the spinal cord of *Mbp-Cre;Ddx20* cKO mice at P42. (a–d) Electron microscopic analyses in the lateral funiculus of control (a,c) and *Mbp-Cre;Ddx20* cKO spinal cords (b,d) at P42 (n=3 mice in each genotype). Thin myelin sheath was observed in the large-diameter axons in the *Ddx20* cKO mice. Scale bars: 20 μm (a,b), 2 μm (c,d). (e,f) G ratio analyses in small-diameter axons (< 2μm) (e) and large-diameter axons (> 2μm). The large-diameter axons have thin myelin in the *Ddx20* cKO mice. Statistics. The number of measured axons is indicated in the bottom. ***, $p<0.001$; n.s., not significant in U-tests.

FIGURE 6 Erk1/2 activation is reduced in the oligodendrocytes of the *Ddx20* cKO mice.

(a,b) IHC for pMAPK in control and *Mbp-Cre;Ddx20* cKO spinal cords at P42. Insets show the high-magnification images of pMAPK-positive cells. Black arrowheads indicate the pMAPK-positive signals. Blue arrows indicate the pMAPK-positive astrocytic processes. Scale bar, 50 μm. (c) Double IHC for pMAPK and PLP in the ventromedial funiculus of control and *Ddx20* cKO spinal cords at P42. (d) Double IHC for pMAPK and Neurofilament-H. Arrowheads indicate the axons (green) wrapped with pMAPK-positive myelin structures (red). (e) Bar charts showing the average number of the axons wrapped with pMAPK-positive OLs in the anterolateral funiculus of control and *Ddx20* cKO spinal cords (per 0.05 mm^2, mean ± SEM, n=3 mice per group). Statistical analysis was performed by two-tailed, unpaired *t*-test. *, $p<0.05$. Scale bars: 50 μm (a–c), 25 μm (d).

FIGURE 7 Responses of astrocytes and microglia in the spinal cord of *Mbp-Cre;Ddx20*

cKO mice.

(a–d) GFAP IHC in the transverse sections of control (a,c) and *Ddx20* cKO (b,d) spinal cords at P42 (n=3 mice in each genotype). (e) Western blot analysis using anti-GFAP antibody in the spinal cords at P42 (n=3 mice in each genotype). β-actin was used as a loading control. Bar chart shows the ratio of GFAP protein levels in Ddx20 cKO spinal cords to those in control spinal cords. The density of GFAP was normalized against that for β-actin. The density of the bands indicated by the red arrowheads was measured. (f,g) GS IHC in the transverse sections of control (f) and *Ddx20* cKO (g) spinal cords at P42 (n=3 in mice each genotype). (h,i) Iba1 IHC in the transverse sections of control (h) and *Ddx20* cKO (i) spinal cords at P42 (n=3 mice in each genotype). (j,k) CD11b IHC in the transverse sections of control (j) and *Ddx20* cKO (k) spinal cords at P42 (n=3 in each genotype). (l–o) Immunohistochemical images showing the activated microglia engulfing myelin in *Ddx20* cKO brains at P42. Double immunostaining for Iba1 and PLP (l, m) or CD68 and MBP (n, o) was performed (n=3 in each genotype). White arrowheads indicate myelin fragments phagocytosed by activated microglia. Statistical analysis was performed by two-tailed, unpaired *t*-test. **, $p<0.01$. Scale bars: 100μm (a,b), 50μm (c,d,f–k), 20μm (l–o).

Supplementary FIGURE 1 Investigation of Ddx20 expression in neurons, astrocytes, and oligodendrocytes in mouse spinal cords.

(a–j) Double-immunostaining for Ddx20 and NeuN (a–c), Ddx20 and GS (d–f), or Ddx20 and Olig2 (g–i) was performed in wild-type spinal cords at P42. Scale bars, 100 μm (a–i).

Supplementary FIGURE 2 Assessment of Cre recombination in oligodendrocyte lineage.

(a–e) GFP reporter gene expression was examined on the parasagittal sections of *Mbp-Cre;Z/EG* brainstems at P14. (a) Confocal images of double IHC for GFP and CC1, a mature oligodendrocyte marker. (b) Confocal images of double IHC for GFP and GFAP, an astrocyte marker. (c) Confocal images of double IHC for GFP and Iba1, a microglia marker. (d) Confocal images of double IHC for GFP and NeuN, a neuronal marker. Scale bars: 50 μm.

Supplementary FIGURE 3 Oligodendrocytic gene expression in the *Mbp-Cre;Ddx20* cKO mice at P21.

(a,b) *Plp* ISH in the transverse sections of control (a) and *Ddx20* cKO (b) spinal cords at P21 (n=3 mice in each genotype). (c,d) *Mbp* ISH in the transverse sections of control (a) and *Ddx20* cKO (b) spinal cords at P21 (n=3 mice in each genotype). (e,f) *Pdgfrα* ISH in the transverse sections of control (e) and *Ddx20* cKO (f) spinal cords at P21 (n=3 mice in each genotype). (g,h) *Gpr17* ISH in the transverse sections of control (g) and *Ddx20* cKO (h) spinal cords at P21 (n=3 mice in each genotype). (i) RT-qPCR analyses of oligodendrocytic genes at P21 (n=3 mice in each genotype). *Actb* was used as an internal control. Statistical analysis was performed by two-tailed, unpaired *t*-test. n.s., not significant. Scale bars: 100 μm (a–h).

Supplementary FIGURE 4 Decreased number of CC1-positive mature oligodendrocytes in the spinal cord of *Mbp-Cre;Ddx20* cKO mice.

(a,b) CC1 IHC in the transverse sections of control (a) and *Ddx20* cKO (b) spinal cords

at P42 (n=3 in each genotype). (c) Bar charts showing the average number of CC1-positive mature OLs in the anterolateral funiculus (per 0.05 mm^2, mean ± SEM, n=3 in each genotype). (d,e) PLP IHC in the transverse sections of control (d) and *Ddx20* cKO (e) spinal cords at P42 (n=3 mice in each genotype). (f,g) MBP IHC in the transverse sections of control (f) and *Ddx20* cKO (g) spinal cords at P42 (n=3 mice in each genotype). (h) Western blot analysis was performed using anti-MBP antibody in the spinal cords at P42 (n=3 mice in each genotype). β-actin (Actb, 42 kDa) was used as a loading control. Bar chart shows the ratio of MBP protein levels in *Ddx20* cKO spinal cords to those in control spinal cords (mean ± SEM). The MBP protein levels were obtained by summing the band intensities of the four isoforms (indicated by arrowheads). (i,j) Double IHC for PLP and NF-H in the transverse sections of control (i) and Ddx20 cKO (j) spinal cords at P42. (k,l) Double IHC for MBP and NF-H in the transverse sections of control (k) and Ddx20 cKO (l) spinal cords. Statistical analysis was performed by two-tailed, unpaired *t*-test. ***, $p<0.001$; n.s., not significant. Scale bars, 100 μm (a,b, d–g); 10 μm (i–l).

Supplementary FIGURE 5 Splicing dysregulation of myelin-related genes in *Mbp-Cre;Ddx20* cKO mice.

(a–f) Semi-quantitative RT-PCR for the alternative splicing of *Plp1* (a)*, Mag* (b)*, and Mbp* (c) mRNA in control and *Ddx20* cKO mice at P42 ($n = 3$ mice per group). Bar charts show the ratio of specific exon inclusion or exclusion in each mRNA (b, d, e, mean ± SEM). *, $p<0.05$; ***, $p<0.001$; n.s., not significant. Signal intensities from electrophoretic bands were determined by densitometric measurement using ImageJ software.

Supplementary FIGURE 6 OPC proliferation is unchanged in *Ddx20* KO spinal cords. (a) Diagrams of the experimental timeline for BrdU short-term administration. (b–g) Double IHC for BrdU and NG2 in the transverse sections of control and *Ddx20* cKO spinal cords at P14 after short-term BrdU labeling experiments. Upper- and lower-panels show the images with BrdU immunostaining (b,c) and BrdU+ NG2+ double-immunostaining (e,f), respectively. Insets show representative of BrdU+ NG2+ double-positive cells. Bar charts indicate the average number of BrdU-positive cells (d) or BrdU+ NG2+ double-positive cells per section (g, mean ± SEM, n=3 mice per group). (h) Diagrams of the experimental timeline for BrdU long-term administration. (i–n) Double IHC for BrdU and NG2 in the transverse sections of control and *Ddx20* cKO spinal cords at P42 after long-term BrdU labeling experiments. Upper- and lower-panels show the images with BrdU immunostaining (i,j) and double IHC for BrdU and NG2 (l,m), respectively. Bar charts indicate the average number of BrdU-positive cells (k) per section in control (n=3 mice) and *Ddx20* cKO (n=3 mice) spinal cords (mean ± SEM). Statistical analysis was performed by two-tailed, unpaired *t*-test. n.s., not significant. Scale bars: 100 μm (b,c,e,f,i,j,l,m).

Supplementary FIGURE 7 BrdU incorporation in astrocytes and microglia of control and *Ddx20* cKO spinal cords.

(a) Diagrams of the experimental timeline for BrdU long-term administration. (b–f) BrdU IHC (b,c) and GS and BrdU double IHC (d,e) after long-term BrdU labelling experiments. GS and BrdU double positive cells per section were counted (f) in the control and *Ddx20* cKO mice (n = 3 mice each genotype). Insets indicate representative GS and BrdU-double positive cells. (g–k) BrdU IHC (g,h) and Iba1 and BrdU double IHC (i,j) after long-term

BrdU labelling experiments. Iba1+ BrdU+ double positive cells per section were counted (k) in the control and *Ddx20* cKO mice (n = 3 mice each genotype). Insets indicate representative Iba1 and BrdU-double positive cells. Statistical analysis was performed by two-tailed, unpaired *t*-test. *, $p<0.05$; n.s., not significant. Scale bars: 100 μm (b–e, g–j).

Supplementary FIGURE 8 Apoptosis is induced in the spinal cords of *Ddx20* cKO mice. (a–d) Images showing TUNEL assay in the transverse sections of control (a,c) and *Ddx20* cKO (b,d) spinal cords at P21 (a,b) and P42 (c,d) (n=3 mice in each genotype). (e, f) Bar charts showing the average number of TUNEL-positive cells in (a–d, mean ± SEM). TUNEL-positive cells per section in the anterolateral funiculus of the spinal cords were counted. Statistical analysis was performed by two-tailed, unpaired *t*-test. *, $p<0.05$; n.s., not significant. Scale bars: 20 μm (a–d).

Supplementary FIGURE 9 Myelin structures in the spinal cord of *Ddx20* cKO mice at P14.

(a, b) Electron microscopic images showing the myelin structures in the lateral funiculus of control (a) and *Mbp-Cre;Ddx20* cKO spinal cords (b) at P14 (n=2 mice in each genotype). Scale bar: 2 μm.

Supplementary FIGURE 10 Reaction of astrocyte and microglia in the *Mbp-Cre;Ddx20* cKO mice.

(a–d) GFAP IHC in the transverse sections of control (a,c) and *Ddx20* cKO (b,d) spinal cords at P14 (a,b) and P21 (c,d) (n=3 mice in each genotype). (e–h) Iba1 IHC in the transverse sections of control (e,g) and *Ddx20* cKO (f,h) spinal cords at P14 (e,f) and P21

(g,h) (n=3 mice in each genotype). (i–l) CD11b IHC in the transverse sections of control (i,k) and *Ddx20* cKO (j,l) spinal cords at P14 (i,j) and P21 (k,l) (n=3 mice in each genotype). Scale bars: 50 μm (a–i).

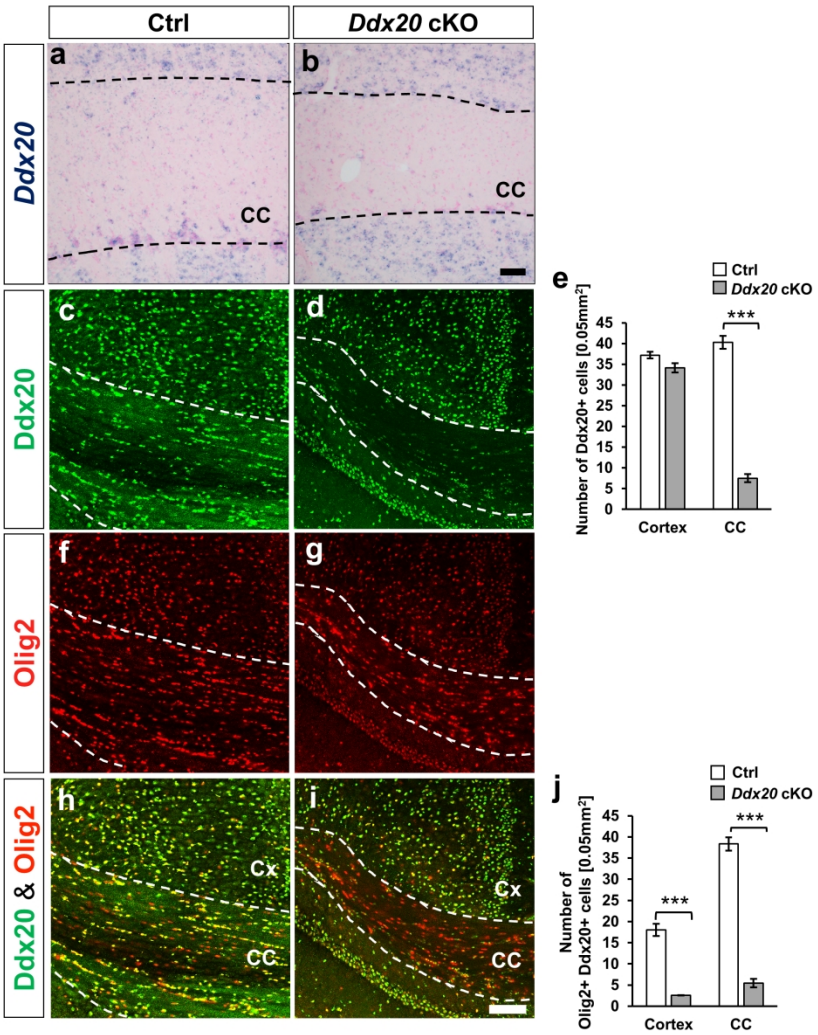

Simankova et al. Fig1

Figure 1

190x275mm (300 x 300 DPI)

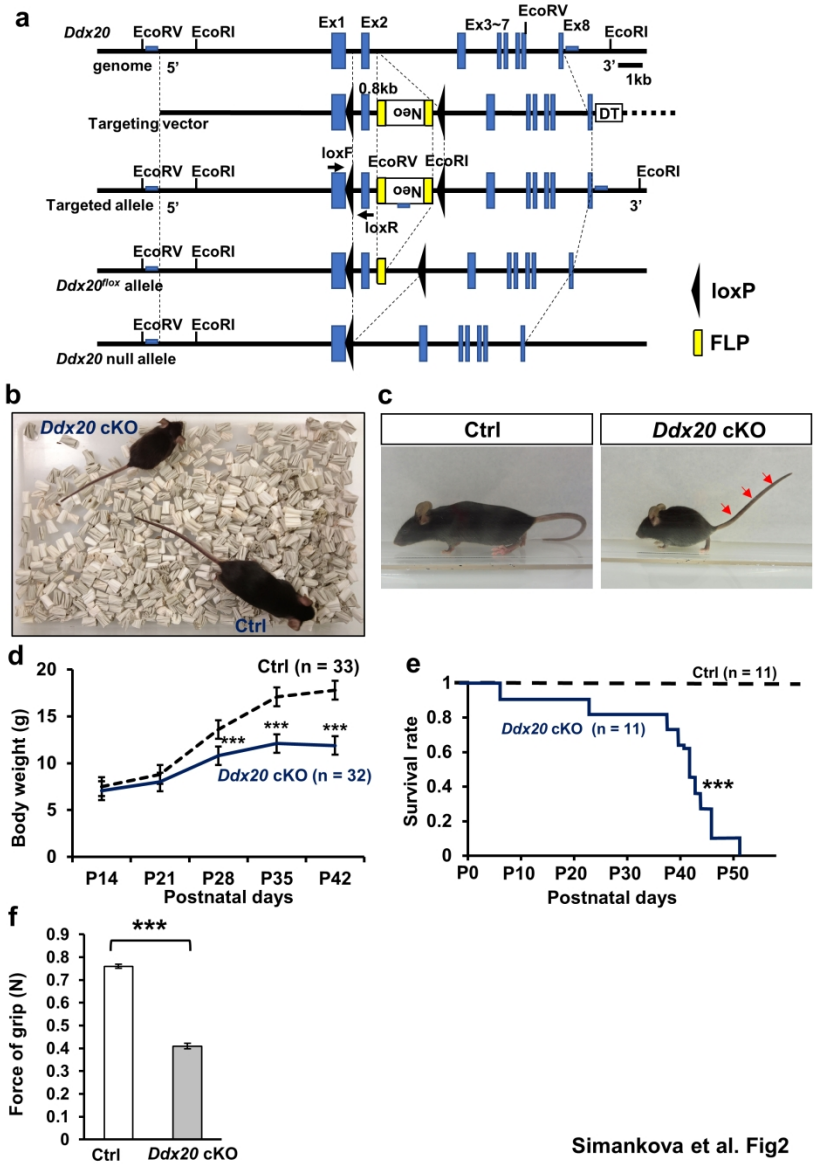

Figure 2

190x275mm (300 x 300 DPI)

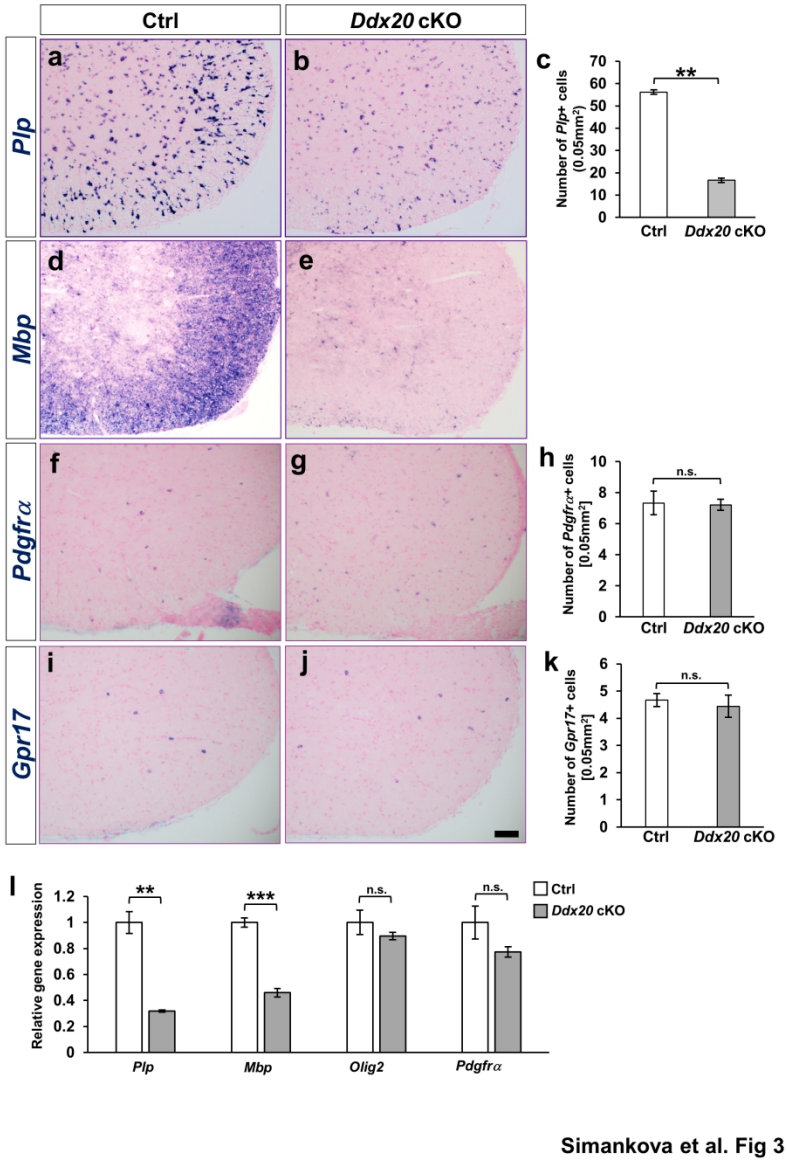

Figure 3

190x275mm (300 x 300 DPI)

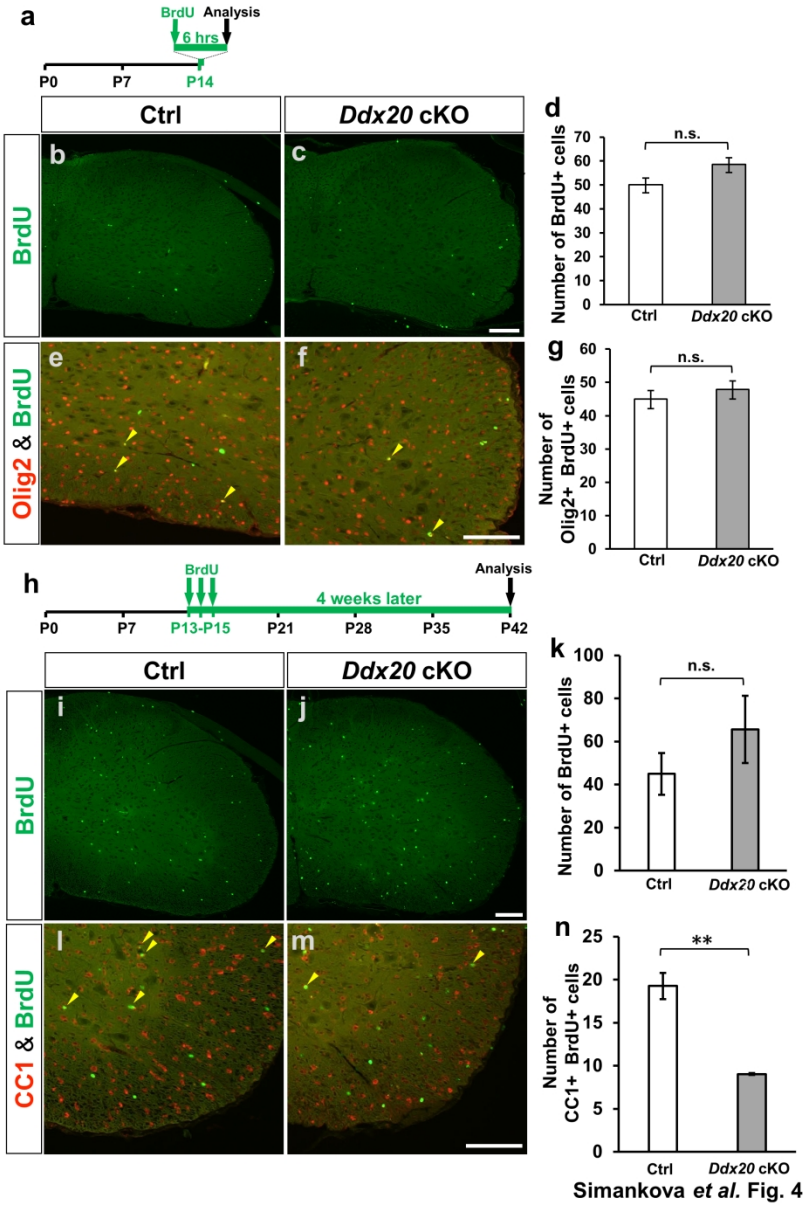

Figure 4

190x275mm (300 x 300 DPI)

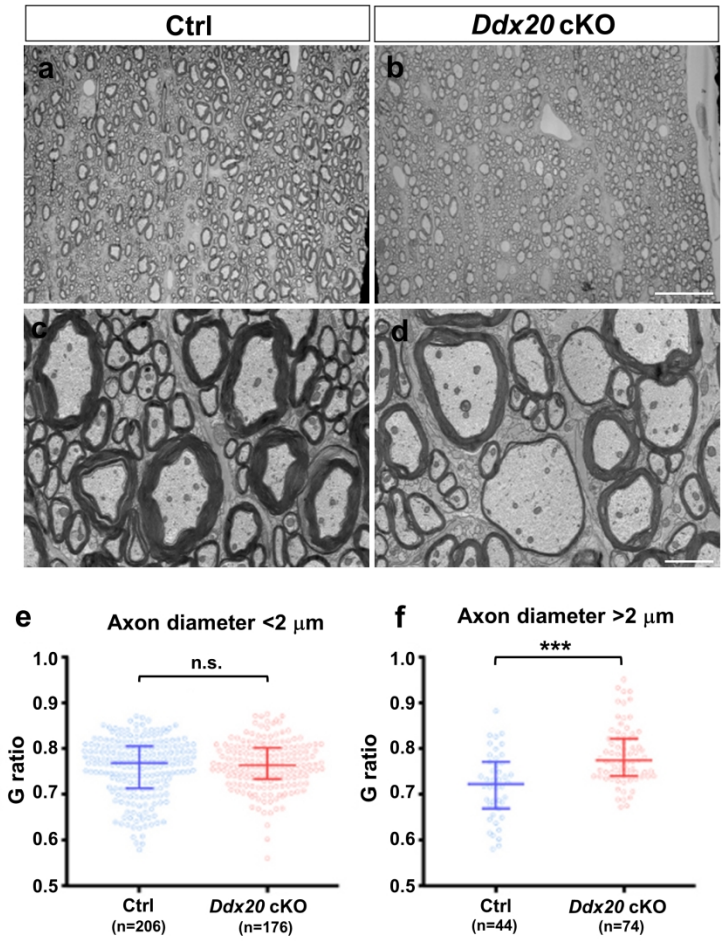

Simankova et al. Fig. 5

Figure 5

190x275mm (300 x 300 DPI)

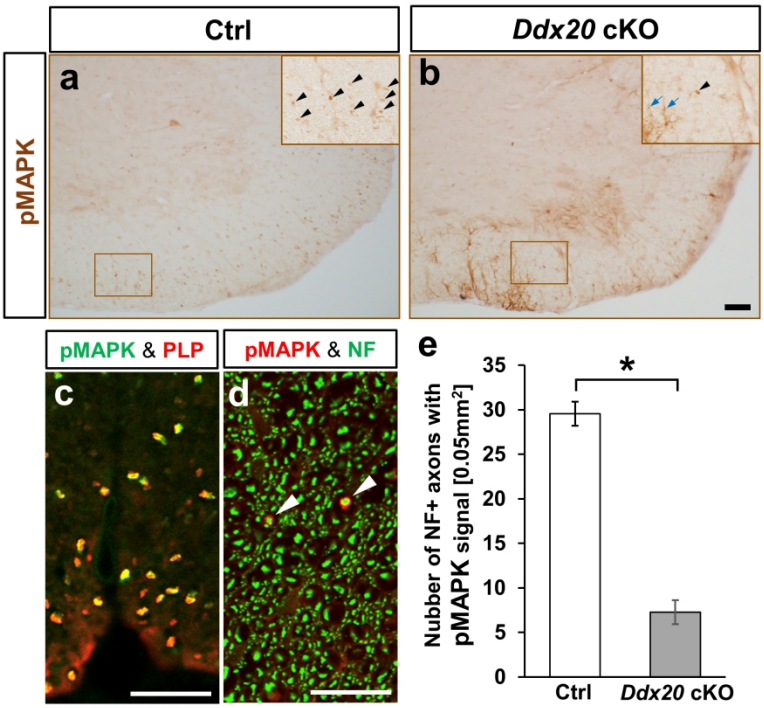

Simankova *et al.* Fig. 6

Figure 6

190x275mm (300 x 300 DPI)

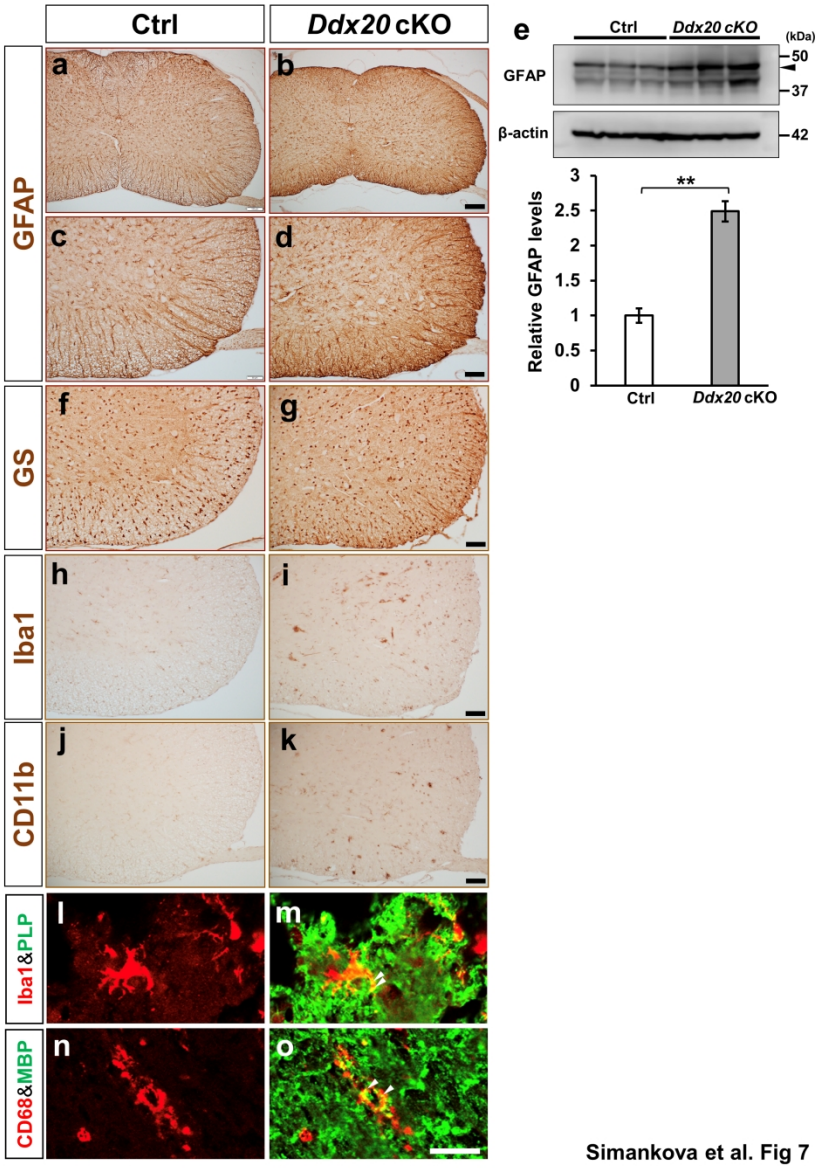

Figure 7

190x275mm (300 x 300 DPI)

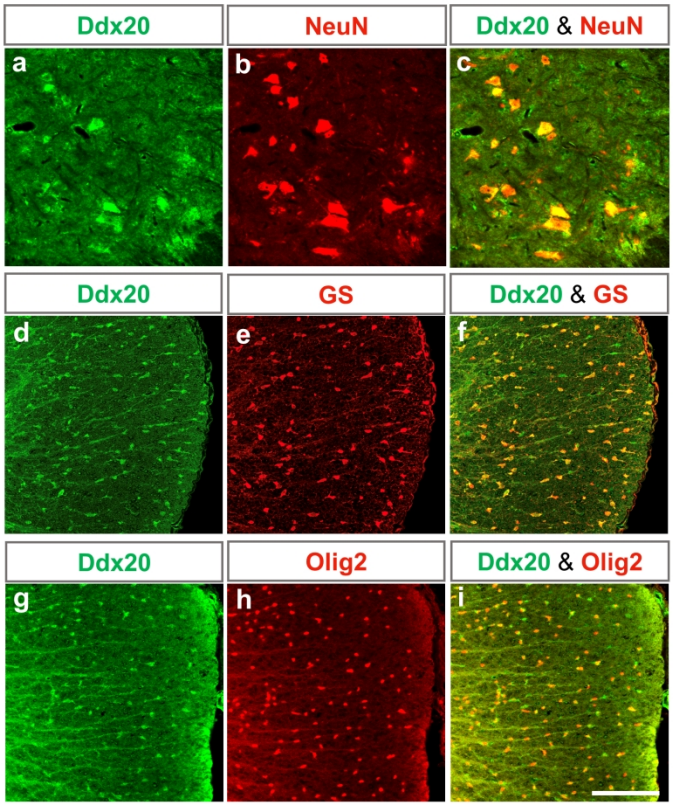

Simankova *et al.* supplementary Fig.1

190x275mm (300 x 300 DPI)

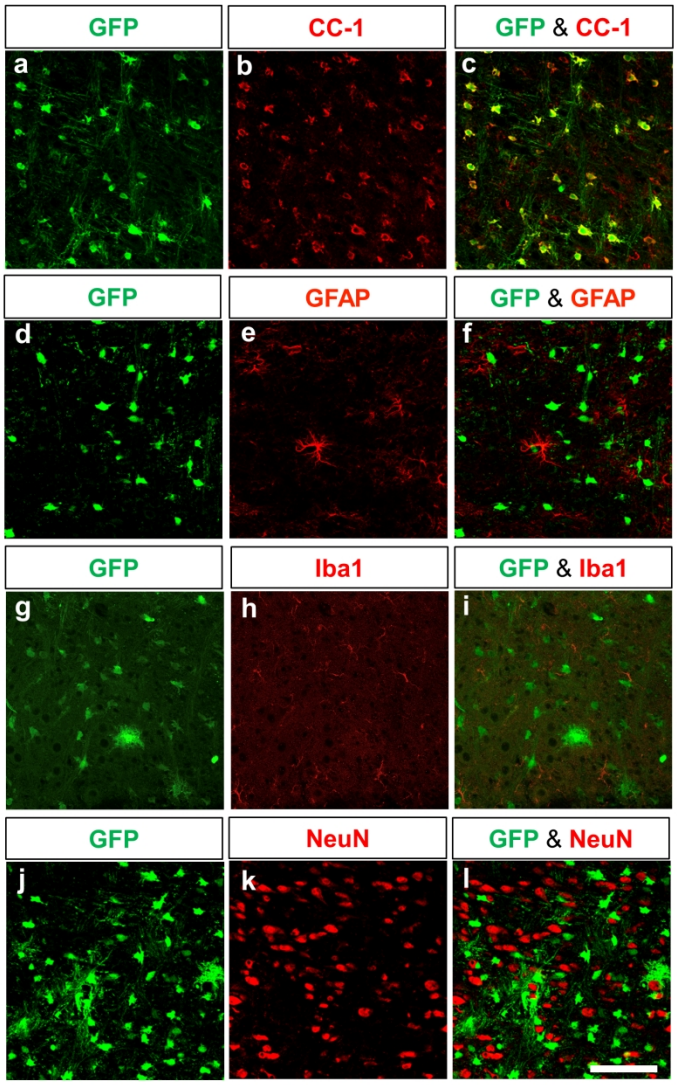

Simankova *et al.* supplementary Fig. 2

190x275mm (300 x 300 DPI)

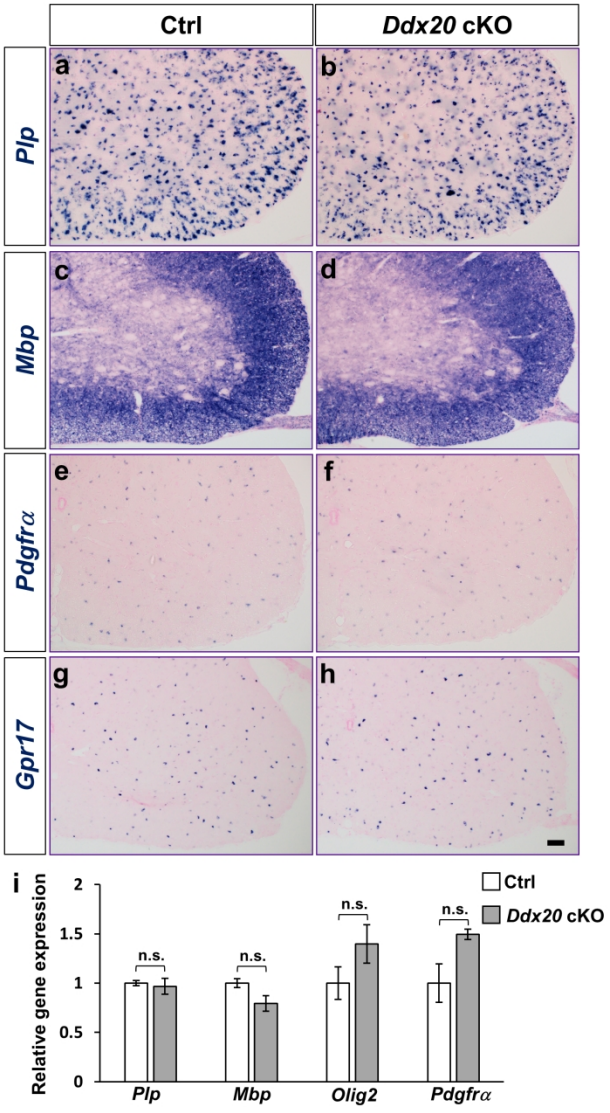

Simankova *et al.* supplementary Fig. 3

190x275mm (300 x 300 DPI)

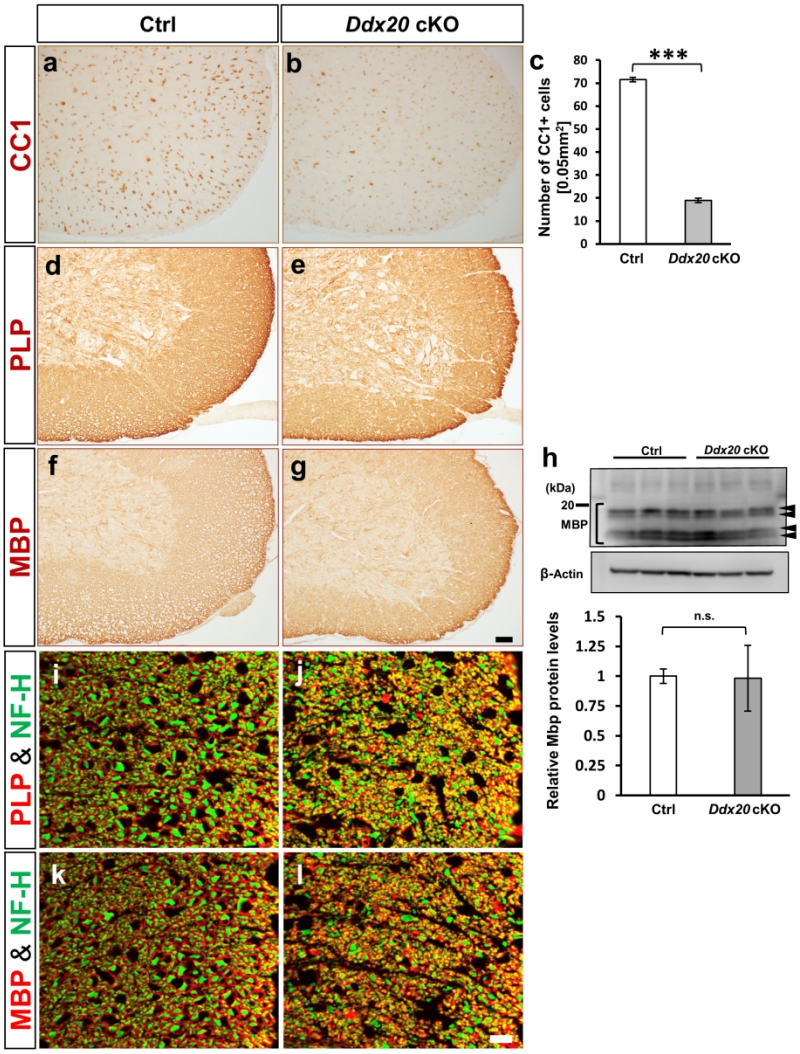

Simankova *et al.* supplementary Fig. 4

190x275mm (300 x 300 DPI)

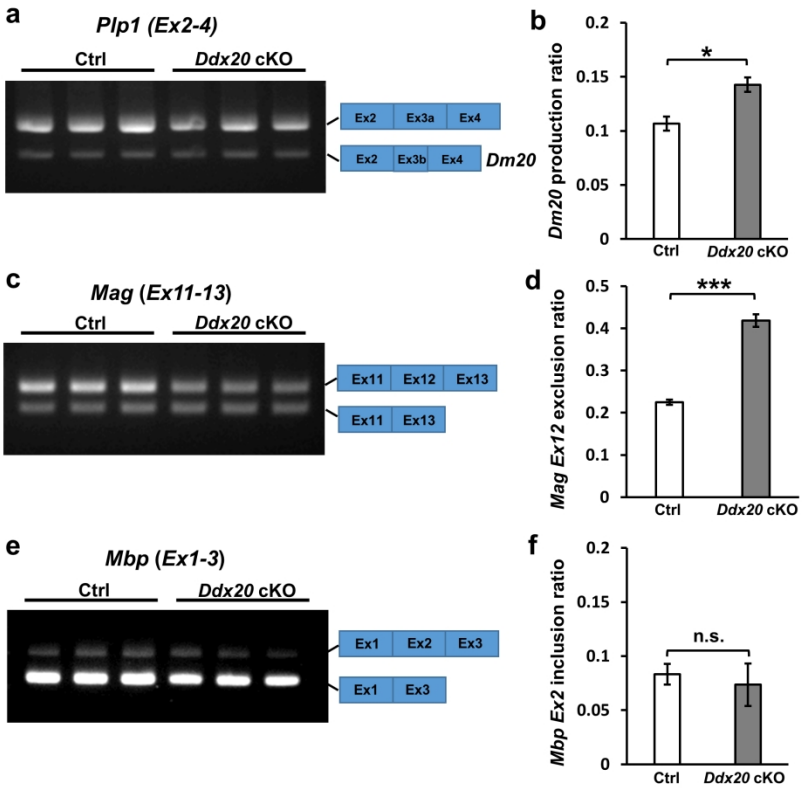

Simankova *et al.* Supplementary Fig. 5

190x275mm (300 x 300 DPI)

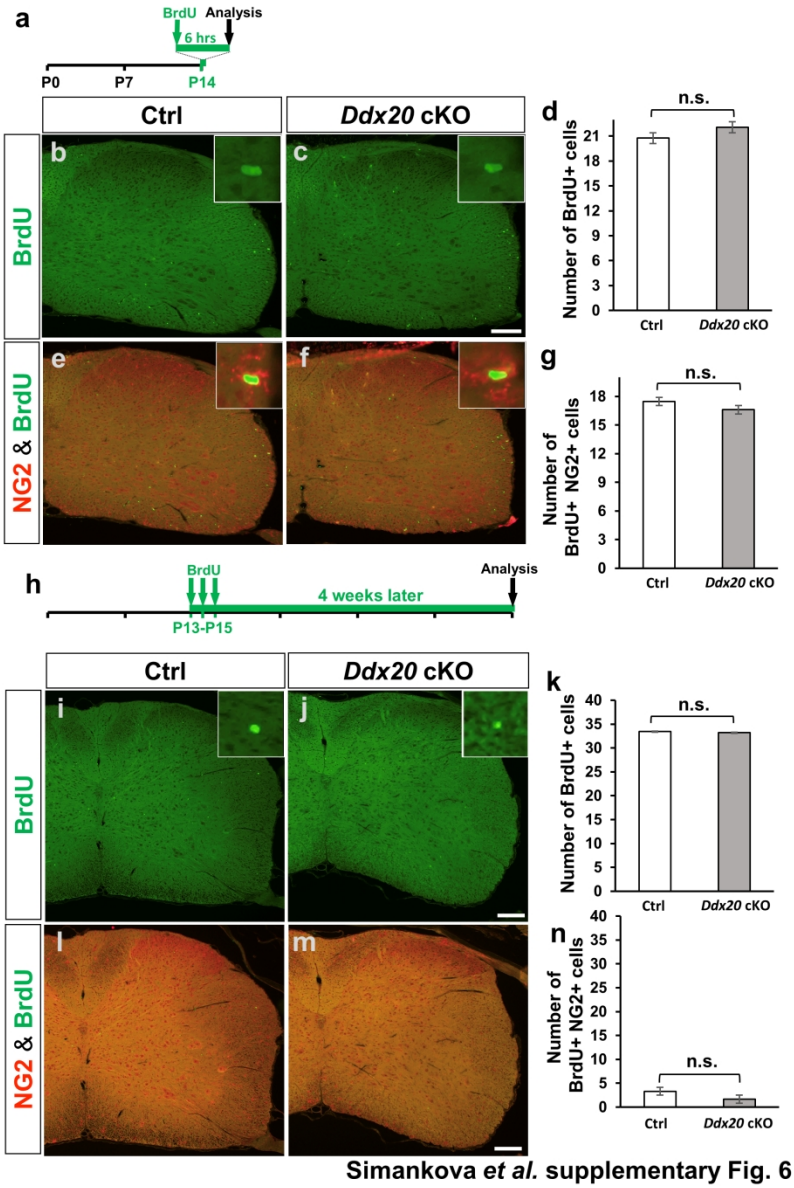

Simankova *et al.* supplementary Fig. 6

190x275mm (300 x 300 DPI)

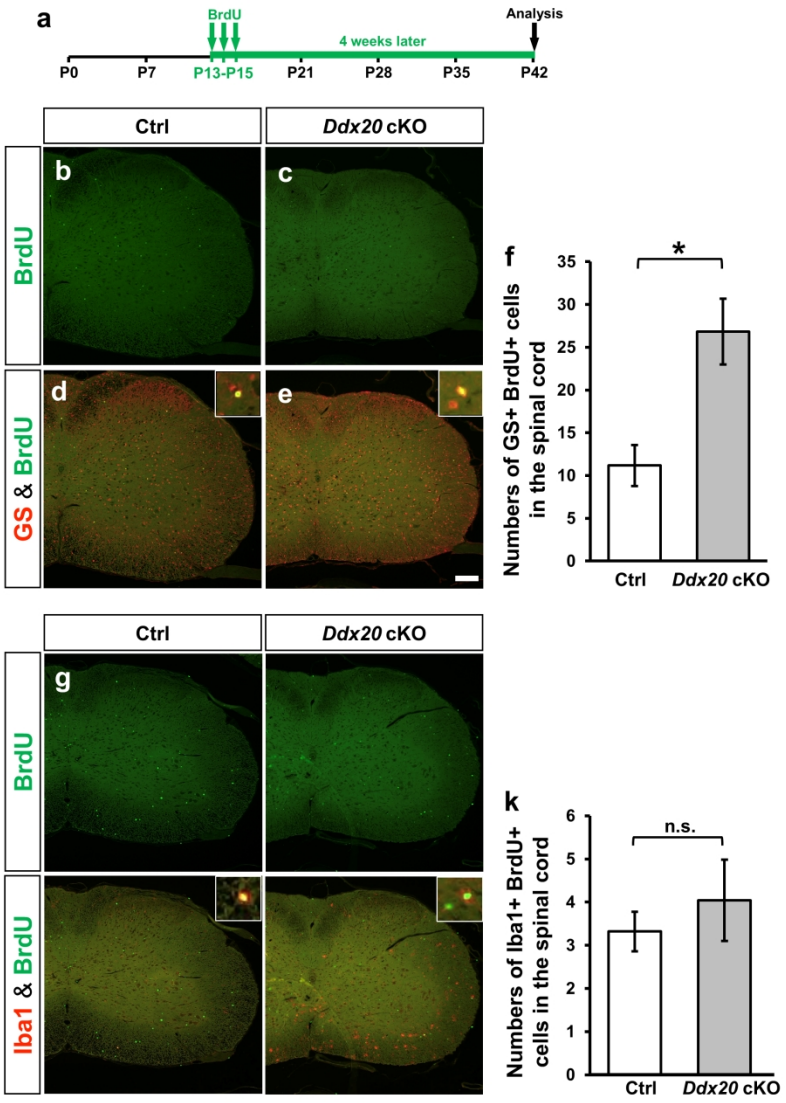

Simankova *et al.* supplementary Fig. 7

190x275mm (300 x 300 DPI)

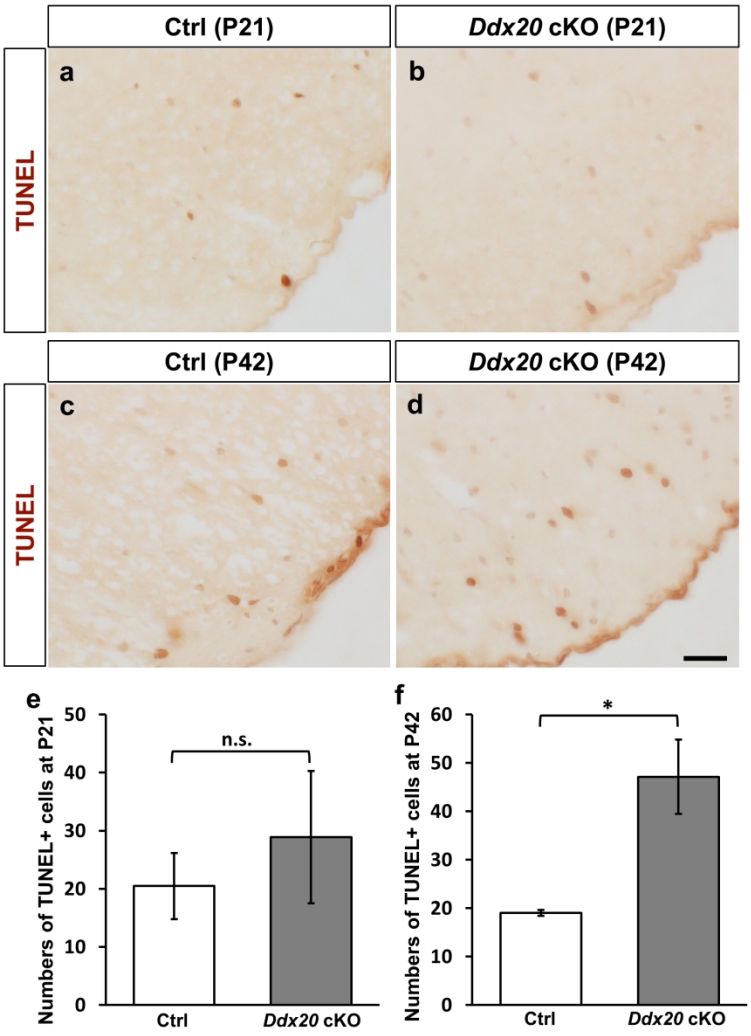

Simankova *et al.* supplementary Fig. 8

190x275mm (300 x 300 DPI)

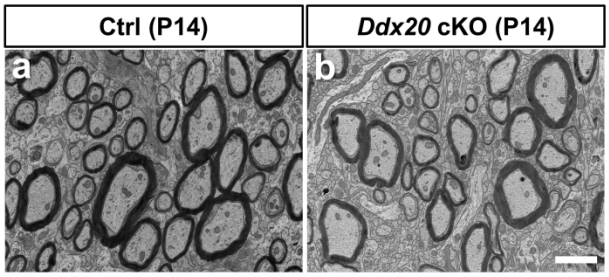

Simankova *et al.* supplementary Fig. 9

190x275mm (300 x 300 DPI)

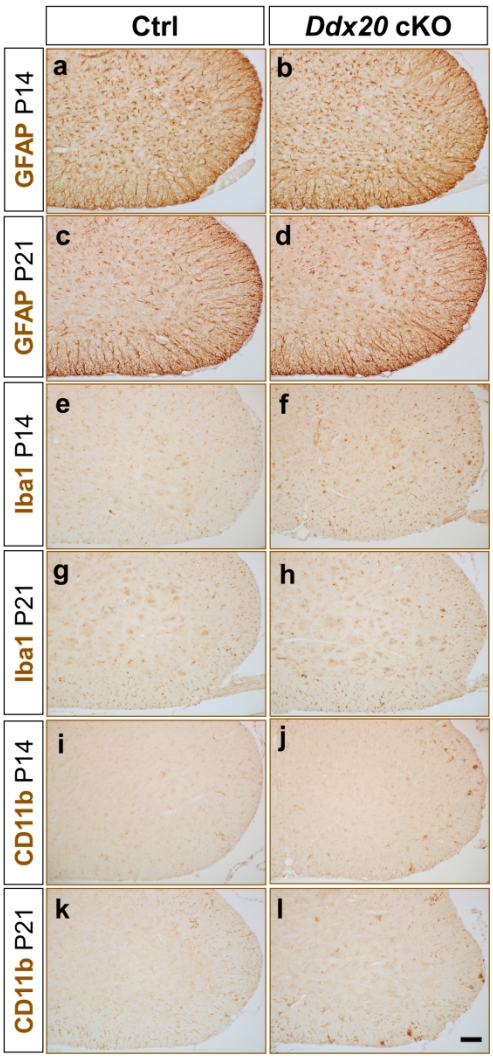

Simankova *et al.* supplementary Fig. 10

190x275mm (300 x 300 DPI)